Materials Horizons

ROYAL SOCIETY OF CHEMISTRY

REVIEW

View Article Online
View Journal | View Issue

Cite this: *Mater. Horiz.*, 2023, **10**, 1901

Vanadium fluorophosphates: advanced cathode materials for next-generation secondary batteries

Shitan Xu,[a] Yi Yang,[a] Fang Tang,[a] Yu Yao,[b] Xiang Lv,[a] Lin Liu,[a] Chen Xu,[c] Yuezhan Feng,[d] Xianhong Rui*[a] and Yan Yu*[b]

Received 2nd January 2023,
Accepted 21st February 2023

DOI: 10.1039/d3mh00003f

rsc.li/materials-horizons

Next-generation secondary batteries including sodium-ion batteries (SIBs) and potassium-ion batteries (PIBs) are considered the most promising candidates for application to large-scale energy storage systems due to their abundant, evenly distributed and cost-effective sodium/potassium raw materials. The electrochemical performance of SIBs (PIBs) significantly depends on the inherent characteristics of the cathode material. Among the wide variety of cathode materials, sodium/potassium vanadium fluorophosphate (denoted as MVPF, M = Na and K) composites are widely investigated due to their fast ion transportation and robust structure. However, their poor electron conductivity leads to low specific capacity and poor rate capacity, limiting the further application of MVPF cathodes in large-scale energy storage. Accordingly, several modification strategies have been proposed to improve the performance of MVPF such as conductive coating, morphological regulation, and heteroatomic doping, which boost the electronic conductivity of these cathodes and enhance Na (K) ion transportation. Furthermore, the development and application of MVPF cathodes in SIBs at low temperatures are also outlined. Finally, we present a brief summary of the remaining challenges and corresponding strategies for the future development of MVPF cathodes.

New concepts

Nowadays, there is an increasing demand for high-energy-density secondary batteries, and thus great efforts have been devoted to searching for suitable electrode materials. As a promising candidate for next-generation batteries, vanadium fluorophosphate has attracted significant attention due to its high voltage plateaus and outstanding structural stability, making its study of significant wider interest. In this review, the current development regarding vanadium fluorophosphate materials as cathodes for sodium/potassium-ion batteries including their basic physicochemical properties and practical application is discussed. Specifically, the relationship between their crystal structure and performance together with their internal energy storage mechanism are explored in-depth, and the achievements from their modification are summarized in detail together with their application at low temperature. In the future, advanced characterization tools are encouraged to exploit and analyze the fine mechanisms of Na/K (de)intercalation, and then optimizing the structures to boost the energy density. Notably, considerable endeavours are necessary to improve the subzero-temperature performance of vanadium fluorophosphates. The insight from this review will contribute to the further development of high-energy-density cathodes in the field of large-scale energy storage.

1. Introduction

Lithium-ion batteries (LIBs) have been widely used in smart devices and hybrid electric vehicles for a long time, occupying a large market share on account of their long service life, high energy storage density, and high operating voltage.[1–10] However, LIBs are associated with some inescapable challenges such as low lithium reserves and high cost, and thus it is necessary to explore alternatives to LIBs. Therefore, SIBs and PIBs have emerged as promising candidates due to their abundant resources, low cost, and high safety.[11–22] Nevertheless, their comprehensive performance cannot match that of LIBs at present mainly owing to the larger radius of Na^+ (∼1.02 Å) and K^+ (∼1.38 Å) than Li^+ (∼0.76 Å), making it more difficult for Na^+/K^+ to diffuse in/out of the electrodes.[23–32] Nowadays, the commercialization of SIBs/PIBs is hindered by their low energy density and inferior cycling stability. Firstly, the phenomenon of low energy density primarily originates from the high redox potential of Na/Na^+ (K/K^+) and their high

---

[a] *Guangdong Provincial Key Laboratory on Functional Soft Condensed Matter, School of Materials and Energy, Guangdong University of Technology, Guangzhou 510006, China. E-mail: xhrui@gdut.edu.cn*

[b] *Hefei National Research Center for Physical Sciences at the Microscale, Department of Materials Science and Engineering, CAS Key Laboratory of Materials for Energy Conversion, University of Science and Technology of China, Hefei, Anhui 230026, China. E-mail: yanyumse@ustc.edu.cn*

[c] *Academy for Advanced Interdisciplinary Studies, Southern University of Science and Technology, Shenzhen 518055, China*

[d] *Key Laboratory of Materials Processing and Mold (Ministry of Education), Zhengzhou University, Zhengzhou 450002, China*

atomic mass, and thus the SIB/PIB cathode materials will lose 15–20% of their theoretical energy density compared to LIBs. Besides, they exhibit inferior cycling stability due to the serious volume dilatation or even structural sabotage after irreversible Na^+/K^+ (de)insertion.[33–37] Thus, the development of advanced cathodes with high energy performance and great cyclability becomes a great challenge to achieve high-performance SIBs/PIBs, which is significant to realize their practical applications.

To date, numerous cathode materials for SIBs/PIBs have been studied, ranging from layered-transition-metal oxides,[38–42] polyanionic compounds,[43–45] and Prussian blue and its analogues[46–49] to organic polymers.[50–52] Nevertheless, their intrinsic deficiencies hinder their full application potential. For instance, some Na^+/K^+-transition metal oxides (*e.g.*, $NaCoO_2$, $Na_{0.44}MnO_2$, and K_xMO_2 (M = Co, Mn, *etc.*)) cannot withstand the conspicuous structural variations derived from the process of repeated Na^+/K^+ (de)insertion, causing significant polarization and capacity degradation, resulting in an inferior electrochemical performance.[53–56] Furthermore, some olivine-type materials (*e.g.*, $NaFePO_4$ and $KFePO_4$) endure sluggish diffusion kinetics for migration of Na^+/K^+ and large lattice mismatch between $NaFePO_4(KFePO_4)$ and $FePO_4$, leading to a poor rate performance and unsatisfactory lifespan.[57,58] Organic polymers have a low specific discharge capacity and poor cyclability due to their dissolution reactions with the electrolyte, which are difficult to meet the actual needs of rechargeable equipment.[59] Accordingly, given that the limitations of the cathode hinder the fabrication of advanced next-generation batteries, significant effort has been devoted to the development and enhancement of cathodes for SIBs/PIBs.[60] In short, there is an urgent demand to explore suitable cathode materials for SIBs/PIBs. Among the different types of materials, NASICON-type vanadium fluorophosphate materials are very popular due to their remarkable structural and thermodynamic stability, large voids, and high energy density ($\sim$500 W h kg^{-1}),[61–65] which make them promising candidates for SIBs (PIBs). In this case, the significant members of the sodium vanadium fluorophosphate family including $NaVPO_4F$, $Na_3V_2(PO_4)_2F_3$ (NVPF), $Na_3V_2O_2(PO_4)_2F$ (NVPOF), and $Na_3V_2O_{2-2x}(PO_4)_2F_{1+2x}$ ($0 < x < 1$) and potassium vanadium fluorophosphate family such as $KVPO_4F$, $K_3V_2(PO_4)_2F_3$ (KVPF) and $K_3V_2O_2(PO_4)_2F$ (KVPOF) have been extensively studied. The F atom is employed to substitute PO_4 given that the fluorine is lighter and carries higher electronegativity (compared to phosphate), finally improving the specific capacity and working voltage plateau of the cathodes. Due to the different contents of F^- and $PO_4{}^{3-}$, the crystal structure and electrochemical properties of these vanadium fluorophosphate materials are very different. For instance, NVPF possesses a higher working voltage than that of NVPOF on account of the presence of more highly electronegative F^- in the former; however, a very high content of F^- will block the migration of Na^+, resulting in sluggish interfacial reaction kinetics. This is the same for KVPF and KVPOF materials. Also, the proportion of O in NVPOF (KVPOF) is higher together with a decrease in the content of F, reducing the bonding with Na^+/K^+ and accelerating the migration of Na^+/K^+, and thus the rate tolerance of NVPOF (KVPOF) is better than that of NVPF (KVPF). In this case, making full use of the benefits and avoiding the disadvantages of F have become a very important issue.

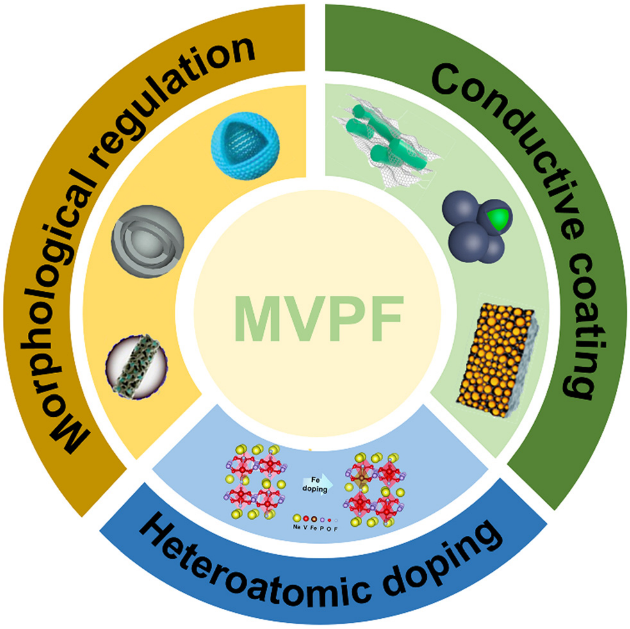

Fig. 1 Schematic of the strategies to prepare MVPF.

In the literature to date, most reviews only focused on the development of polyanionic materials for application in SIBs (PIBs) and rarely vanadium fluorophosphate-type cathode materials. Thus, in this review, we systematically summarize the basic crystal structure, Na^+/K^+ storage mechanism, modification strategies, and the electrochemical performance of vanadium fluorophosphate-type cathodes (Fig. 1). Eventually, the major challenges and corresponding strategies for the development of vanadium fluorophosphate materials are proposed, aiming to provide some meaningful inspiration for the development of vanadium fluorophosphate materials for SIBs/PIBs.

2. Crystal structure and Na/K storage mechanism

2.1 Sodium vanadium fluorophosphates

2.1.1 $NaVPO_4F$. $NaVPO_4F$ possesses two categories of crystal structures that have Na storage capacity, *i.e.*, tetragonal structure (space group: *I*4/*mmm*) and monoclinic structure (space group: *C*2/*c*).[66–69] Tetragonal-structured $NaVPO_4F$ shows an extended 3D framework consisting of $[VO_4F_2]$ octahedra and $[PO_4]$ tetrahedra for Na^+ diffusion, operating at 3.8 V *vs.* Na^+/Na and demonstrating a higher Na-storage capability. It was previously reported that $NaVPO_4$ undergoes a transition from tetragonal phase to monoclinic phase at high temperatures.[70] In the monoclinic-$NaVPO_4F$, two PO_4 tetrahedra are connected to two VO_4F_2 octahedra by two angular oxygen atoms, and Na^+ possesses a 2D pathway along the (010) plane. The monoclinic-$NaVPO_4F$ can realize the reversible extraction/insertion of one

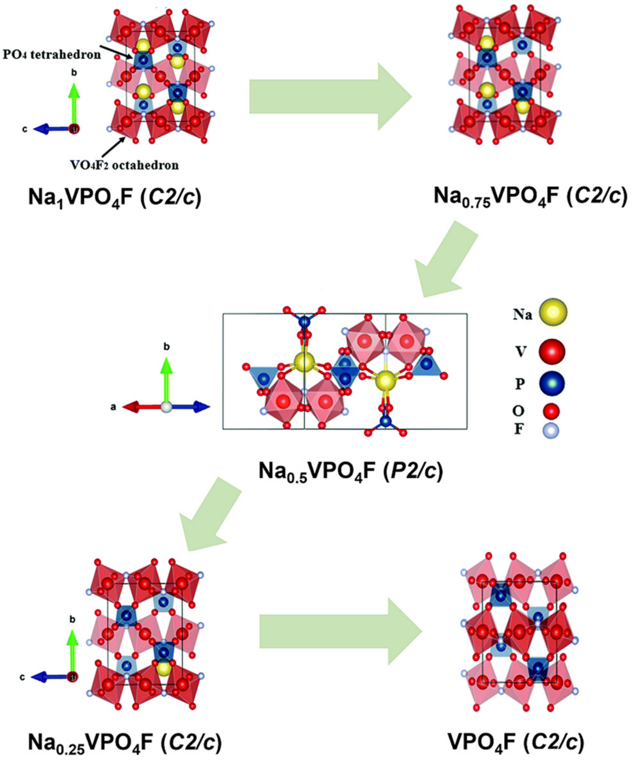

Fig. 2 Evolution process of $NaVPO_4F$ space group during desodiation. Reproduced with permission.[66] Copyright 2019, The Royal Society of Chemistry.

Na^+ per $NaVPO_4F$ formula unit induced by the V^{4+}/V^{3+} redox reaction, showing a theoretical capacity of 143 mA h g^{-1} and working plateau of $\sim$3.4 V, which prevents further improvement in its energy density.[71] Furthermore, it has been confirmed that $NaVPO_4F$ possesses a stable 3D tunnel-like structure, which offers abundant interstitial pathways for Na^+ transportation and mitigates the large volume expansion during cycling. The desodiation process can be analysed by removing Na^+ from $Na_{1-x}VPO_4F$ with the parameter x = 0, 0.25, 0.5, 0.75, and 1. As shown in Fig. 2, the evolution process of the space group follows the order of Na_1VPO_4F ($C2/c$) → $Na_{0.75}VPO_4F$ ($C2/c$) → $Na_{0.5}VPO_4F$ ($P2/c$) → $Na_{0.25}VPO_4F$ ($C2/c$) → VPO_4F ($C2/c$). Significantly, the structural symmetry of $NaVPO_4F$ shifts from the $C2/c$ space group to the $P2/c$ space group when 0.5 Na^+ is extracted. This phase transition may be due to the remarkable difference in the bond length between the $C2/c$ and $P2/c$ space groups.

2.1.2 $Na_3V_2(PO_4)_2F_3$.

The exploration of the crystal structure of $Na_3V_2(PO_4)_2F_3$ revealed that NVPF possesses a tetragonal structure (space group: $P4_2/mnm$; cell parameters: a = b = 9.047 Å and c = 10.749 Å.), and the $[V_2O_8F_3]$ bi-octahedra and $[PO_4]$ tetrahedra are interconnected by angle sharing (Fig. 3a). In the NVPF frame structure, the occupancy ratio between the Na(1) sites and Na(2) sites is 2 : 1. Fig. 3b reveals the evolution of the NVPF space group during desodiation, and the phase diagram stabilized in the composition range of $Na_3V_2(PO_4)_2F_3$ to $Na_1V_2(PO_4)_2F_3$ is a complex succession of biphasic and solid solution-type reactions. On account of the electronegativity of fluorine, the high fluorine content in the $Na_3V_2(PO_4)_2F_3$ cathode results in high redox potentials of 3.9 V and 4.3 V for desodiation and sodiation, respectively.[72–77] The electrochemical reaction of $Na_3V_2(PO_4)_2F_3$ can be described as the following equations:

$$Na_3V_2(PO_4)_2F_3 \leftrightarrow Na_2V_2(PO_4)_2F_3 + Na^+ + e^- \quad (1)$$

$$Na_2V_2(PO_4)_2F_3 \leftrightarrow Na_1V_2(PO_4)_2F_3 + Na^+ + e^- \quad (2)$$

Most researchers believe that only two Na^+ are involved in the insertion/de-insertion reaction of NVPF in SIBs, while the third Na^+ possesses no electrochemical activity, which hinders the upper limit of their specific capacity. Although the energy density resulting from the high voltage platform is impressive, it is still far from the requirement of practical applications. Therefore, to boost the energy density, activating the electrochemical activity of the third Na^+ is necessary. In this regard, Yan *et al.* designed the disordered structure of $NaV_2(PO_4)_2F_3$ as a cathode for SIBs and found that the third electrochemical activity was successfully activated. Consequently, the last Na^+ is successfully embedded at 1.6 V with a change in the valence state *vs.* Na^+/Na^0. In addition to studying the third sodium deblocking pathway and structural evolution, the test results of full cells are very exciting, and the energy density is expected to increase by 10–20%.[78] This exciting discovery has led to more attention being directed to NVPF. Mukherjee *et al.* used the

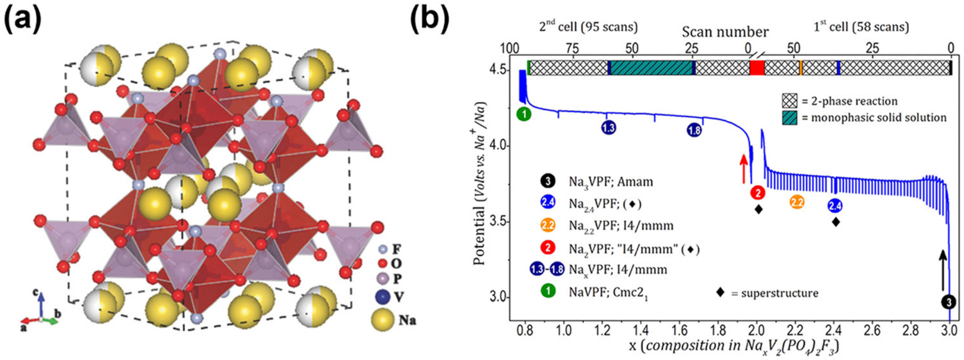

Fig. 3 (a) Crystal structure of $Na_3V_2(PO_4)_2F_3$. Reproduced with permission.[184] Copyright 2018, Wiley-VCH. (b) Phase diagram upon charging $Na||Na_3V_2(PO_4)_2F_3$. Reproduced with permission.[77] Copyright 2015, the American Chemical Society.

solvothermal method to construct hollow sphere $Na_3V_2(PO_4)_2F_3$ as a cathode material for SIBs, which increased the output capacity (~100 mA h g^{-1}) under limited voltage, realizing a high discharge capacity of 197 mA h g^{-1}. These results are attributed to the successful release of the third sodium of the $Na_3V_2(PO_4)_2F_3$ due to the constructed morphology structure.[79] However, stability is still a key problem to be solved to achieve large voltage window applications. In addition to activating the electrochemical activity of the third Na^+, a valid method to increase the theoretical capacity and energy density of $Na_3V_2(PO_4)_2F_3$ is to expand its working voltage window. For instance, Peng *et al.* prepared a nano-$Na_3V_2(PO_4)_2F_3$ cathode material *via* the sol–gel method, and subsequently calcination, where the dispersion of the released gases generated from the decomposition of excess citric acid caused a certain of lattice distortion and defects. Based on the weakening of the electrostatic repulsion between Na^+ in NVPF, the interlayer spacing was subsequently expanded, and more Na^+ could lightly enter the structure and form a new type of $Na_4V_2(PO_4)_2F_3$ material. Consequently, a new plateau at 1.38 V/1.56 V corresponding to the V^{3+}/V^{2+} redox was displayed, resulting in a high discharge capacity of 250 mA h g^{-1}, which surpasses that of the primitive two-electron redox reaction of $Na_3V_2(PO_4)_2F_3$. This confirms that the electrochemical reaction based on the reversible redox of three Na^+ is effective.[80]

2.1.3 $Na_3V_2O_2(PO_4)_2F$. As the representative material in the $Na_3(VO_{1-x}PO_4)_2F_{1+2x}$ ($0 \leq x \leq$ (1) family, $Na_3V_2O_2(PO_4)_2F$ is formed when $x = 0$, which possesses a tetragonal symmetry structure with the space group of *I*4/*mmm* and lattice parameters of $a = b = 6.3810$ Å, $c = 10.5860$ ÅÅ. In $Na_3V_2O_2(PO_4)_2F$ (Fig. 4a), a couple of VO_5F octahedra share a common F-angle and each VO_5F octahedral couple shares all its oxygen vertices with the PO_4 tetrahedral unit. In this framework structure, the interval channels run along the *a*, *b*-axes, and their intersection provides a considerable cavity, where the Na^+ in the interval space runs disorderly at two separate locations with a high degree of separation. This large tunnel structure is beneficial for fast Na^+ transport. The occupation of the Na sites in the NVPOF structure is similar to that in the NVPF material, where two Na^+ are located at the Na(1) site and one at the Na(2) site. The Na^+ in the Na(1) site is slightly shifted away from the center of the prismatic site, while the Na^+ in the Na(2) site is shifted in the opposite direction owing to the repulsion of Na^+ from the adjacent Na(1) site. Therefore, in terms of Na^+ removal from the NVPOF structure, more energy is required from the Na(1) site compared to the Na(2) site.[81–83]

$Na_3V_2O_2(PO_4)_2F$ with weaker inductive effects facilitates Na^+ diffusion, which possesses two high working plateaus at approximately 3.6 V and 4.0 V *vs.* Na/Na$^+$ given that two Na^+ can be (de)inserted reversibly during the GCD process (Fig. 4b). The corresponding two-step extraction/insertion reactions of Na^+ are as follows:

$$Na_3V_2O_2(PO_4)_2F \rightleftharpoons Na_2V_2O_2(PO_4)_2F + Na^+ + e^- \tag{3}$$

$$Na_2V_2O_2(PO_4)_2F \rightleftharpoons Na_1V_2O_2(PO_4)_2F + Na^+ + e^- \tag{4}$$

Moreover, Peng *et al.* adopted a wide operating voltage window (1–4.5 V) to explore the (de)insertion behaviour and evolution in the Na storage mechanism of $Na_3V_2(PO_4)_2O_2F$. The results showed that NVOPF with the space group of *I*4/*mmm* could be intercalated with extra one Na^+ at the slope of 1.5–1.0 V, delivering a high capacity of 180 mA h g^{-1}.[84]

2.1.4 $Na_3V_2O_{2-2x}(PO_4)_2F_{1+2x}$ ($0 < x < 1$). Based on introducing an F anion to construct fluorophosphate, researchers also proposed replacing some F^- with O^2, synthesizing the novel material $Na_3V_2O_{2-2x}(PO_4)_2F_{1+2x}$ ($0 < x < 1$) (also named $Na_3V_2O_{2x}(PO_4)_2F_{3-2x}$). The most common space groups of this type of material are *P*4$_2$/*mnm* and *Amam*. Taking $Na_3V_2O_{2x}(PO_4)_2F_{3-2x}$ ($x = 0.8$) as an example, it processes a space group of *P*4$_2$/*mnm* and the calculated cell parameters of $a = 9.07227(2)$ Å, $c = 10.6593(7)$ Å. In terms of the reaction mechanism of the charge–discharge process, this electrode goes through a short solid solution regime followed by a biphasic region and a second solid solution, which continues until the completion of charge. Specifically, the solid solution accounts for the majority of the initial discharge, and the final part of the low voltage plateau during discharge is composed of a biphasic region with a solid solution section.[85]

2.2 Potassium vanadium fluorophosphates

2.2.1 $KVPO_4F$. As an analog of $KTiOPO_4$, $KVPO_4F$ possesses a very similar crystal structure with subtle difference in the atom used for connecting the metal octahedra.[86,87] In the structure of $KVPO_4F$, VO_4F_2 octahedra are interconnected *via* corner-sharing PO_4 tetrahedra, and the F atom can occupy the equatorial (V1 site) or axial positions (V2 site) around the vanadium atom, as well as the VO_4F_2 octahedron shares the F atom through a common angle, composing zig–zag chains and tightly connected by PO_4 tetrahedra (Fig. 5a).[88] During cycling,

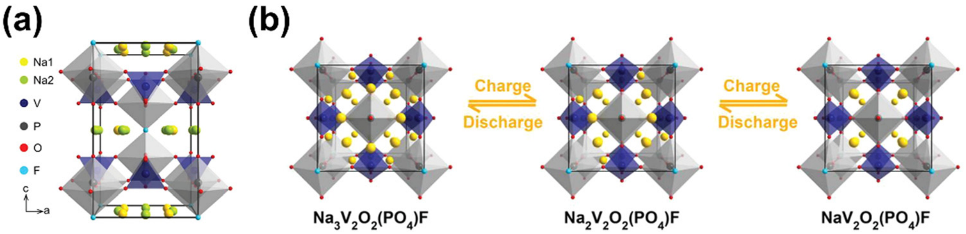

Fig. 4 (a) Crystal structure of $Na_3V_2O_2(PO_4)_2F$ and (b) corresponding evolution of its crystal structure during sodiation/desodiation. Reproduced with permission.[146] Copyright 2020, Wiley-VCH.

the K_xVPO_4F cathode experiences various intermediate phases during K^+ extraction/insertion ($KVPO_4F \leftrightarrow K_{0.75}VPO_4F \leftrightarrow K_{0.625}VPO_4F \leftrightarrow K_{0. 5}VPO_4F \leftrightarrow VPO_4F$), in terms of the phase transition during de-intercalation, which is similar to that of the $NaVPO_4F$ electrode in SIBs.[89]

2.2.2 $K_3V_2(PO_4)_2F_3$ and $K_3V_2O_2(PO_4)_2F$. In addition to the commonly studied $KVPO_4F$ material in K-based vanadium fluorophosphates, the novel $K_3V_2(PO_4)_2F_3$ and $K_3V_2O_2(PO_4)_2F$ materials are also considered promising cathodes in this family. Although there are few relevant studies, researchers have revealed some interesting intrinsic elements. Lin *et al.* proposed the use of Rietveld refinement to investigate the crystal structure and phase composition of the KVPF electrode during the electrochemical processes. Approximately 0.6 K^+ is extricated from the structure to produce a component that approximates to KVPF when the battery is charged to 4.2 V. The corresponding cell parameters were determined to be $a = b = 6.336(1)$ Å, $c = 11.506(3)$ Å. Subsequent charging to a deeper level will cause the removal of the remaining close to one K^+, with the determined formula of $K_1V_2(PO_4)_2F_3$ and *Cmc*21 structure. The unit cell volume after charging to 4.6 V was calculated to be 884.65 Å^3, corresponding to an overall volume change from $K_3V_2(PO_4)_2F_3$ to $K_1V_2(PO_4)_2F_3$ of only $\Delta V/V = 6.2\%$, which is superior to the $LiFePO_4$ cathode with a volume expansion of 7.0% during cycling in LIBs, explaining the good stability of the KVPF cathode over long-term cycling. Zhang *et al.* investigated the possible K^+ transport pathway *via* DFT calculation. As shown in Fig. 5b, there are two sites in the lattice for K^+ accommodation, where K2 is coordinated by only six O atoms and K1 is coordinated by six O atoms and an extra F atom and the presence of the high-electronegativity F generates larger electrostatic forces, making the K1 site more stable than the K2 site. Four possible K^+ diffusion paths (D1, D2, D3 and D4) were detected in the KVPOF crystal structure, among which D1, D2 and D3 are related to the *ab*-plane and D4 the *c*-plane. The D1 path represents the K^+ migration from the K1 site to the adjacent K2 site, while the D4 path refers to the K^+ in pristine K1 sites migrating to the adjacent same K1 site along the *c*-axis. The corresponding migration pathways in the *ab*-plane and *c*-axis are shown in Fig. 5c. Besides, the migration energies of K^+ diffusion in the *ab*-plane were determined to be 33 (D1), 65 (D2) and 58 (D3) meV, respectively. Also, the migration energy along the *c*-axis of the D4 path is as high as 6186 meV, which is challenging for diffusion in this direction (Fig. 5d). According to the calculations, K^+ mainly diffuses in the *ab*-plane and blocked in the *c*-axis direction due to the

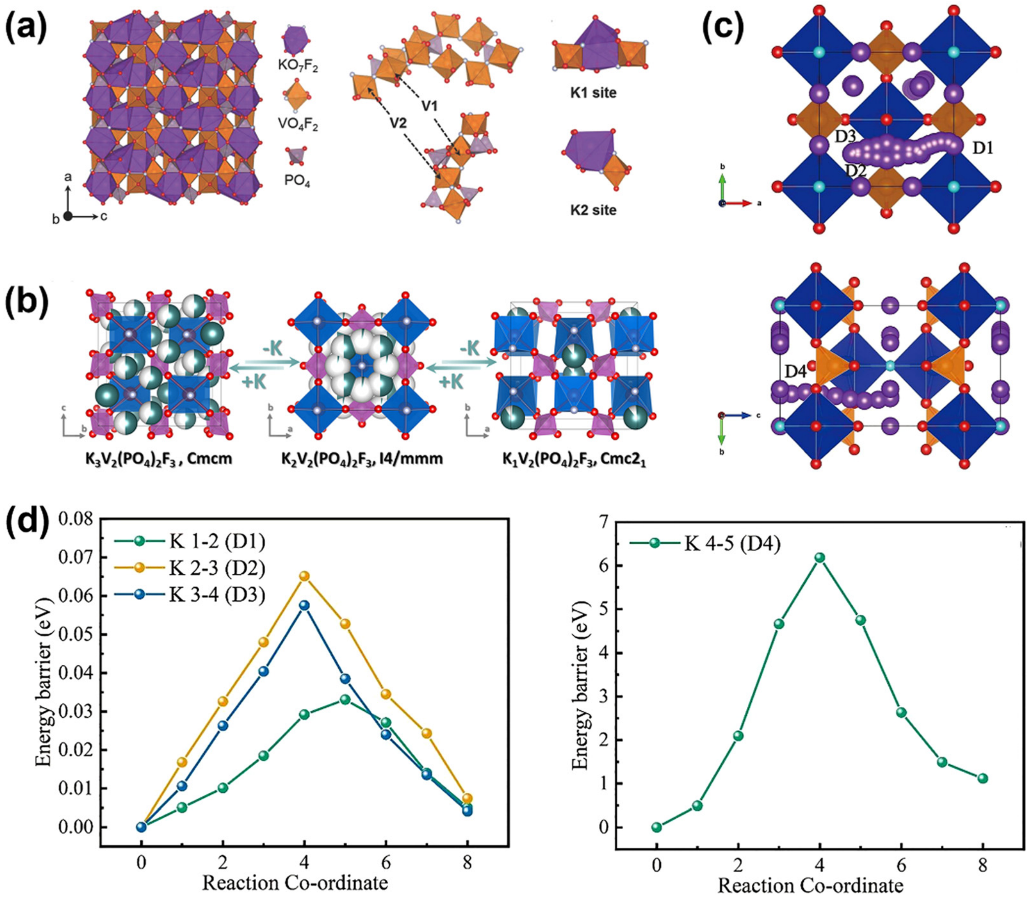

Fig. 5 (a) Crystal structure of $KVPO_4F$. Reproduced with permission.[89] Copyright 2018, Wiley-VCH. (b) Evolution of the crystal structure of $K_3V_2(PO_4)_2F_3$ during (de)potassiation. Reproduced with permission.[159] Copyright 2018, Elsevier. (c) Potential K^+ migration pathways in KVPOF and (d) corresponding energy barriers for K^+ migration. Reproduced with permission.[160] Copyright 2022, Elsevier.

high diffusion activation energy, which is consistent with the NVOPF material.

3. Modification strategies

The introduction of highly electronegative fluorine makes the specific capacity and voltage platform of vanadium fluorophosphate materials more excellent than that of F-free vanadium phosphates, and therefore they are suitable for the constructing of high energy/power density secondary batteries. Unfortunately, vanadium fluorophosphate materials inevitably suffer from low intrinsic electronic conductivity, and thus the diffusion kinetics of Na/K is sluggish, making it difficult to achieve a satisfactory performance in practical applications when used in SIBs/PIBs. Therefore, exploring sophisticated modification techniques for accelerated charge transfer and Na/K diffusion rate in MVPF cathodes is necessary. Incidentally, in the case of K-based materials, there is also the problem of rapid capacity degradation, which may arise from the easy collapse of their structure during cycling.

Thus far, the modification strategies mainly include three categories of compounding with conductive materials, morphological regulation, and heteroatomic doping.[90–92] The incorporation of various carbon materials (amorphous carbon, carbon nanotubes (CNTs), carbon nanofibers (CNF), graphene oxide (GO) and reduced graphene oxide (rGO)) in MVPF-type materials is a convenient and cost-effective strategy for enhancing their properties.[18,93–96] The carbons act as reducing agents to reduce the high valence vanadium and conductive additives to improve the electronic conductivity and minimize the polarization of batteries. Furthermore, the presence of carbon will inhibit the overgrowth and aggregation of the MVPF nanograins during calcination. Moreover, a uniform carbon coating can effectively prevent the micro-dissolution caused by direct contact with the electrode/electrolyte and reduce the interfacial impedance. Also, morphological regulation such as the construction of micro-nano grading structures can shorten the diffusion length between Na^+ and electrons, enhance the diffusion efficiency and enhance the electrochemical performance, while also preventing electrochemical agglomeration. In addition, the construction of nanostructures can effectively shorten the diffusion path of Na^+/K^+ and increase the contact area between the electrode and electrolyte, promoting the kinetics of the electrochemical reaction.[97] Heteroatomic doping usually plays a role in expanding the lattice spacing of materials, making the ex/intercalation of Na^+/K^+ easier, and finally achieving improved diffusion dynamics and stabilizing the crystal structure by using the columnar support of heteroatoms.[98] The current modification strategies, modification effectiveness, progress, and existing problems associated with different sodium (potassium) vanadium fluorophosphate materials will be introduced below.

3.1 Sodium vanadium fluorophosphates

3.1.1 $NaVPO_4F$. $NaVPO_4F$ has a high theoretical capacity of 143 mA h g^{-1}, working plateau of 3.4 V *vs.* Na/Na^+ and high safety, but still exhibits some inevitable problems. For example, its electrochemical properties are significantly hindered by its poor electronic conductivity, and thus $NaVPO_4F$ still suffers from unsatisfactory specific capacity, inferior rate capability, and short lifespan in practical applications. Therefore, enhancing the diffusion kinetics of electron and Na^+ transfer in $NaVPO_4F$ is necessary.[99,100]

To achieve faster Na^+/e^- diffusion, various strategies have been applied to modify $NaVPO_4F$, including carbon coating, constructing nano-micro morphology in materials, and doping with heteroatoms. A carbon coating can ensure the structural integrity upon repeated (de)insertion, elevating the intrinsic electronic conductivity of fluorophosphate materials, and consequently their rate performance and cyclability are enhanced. For example, Ling *et al.* adopted a ball-mining method to synthesize an $NaVPO_4F$@C material. The as-prepared $NaVPO_4F$@C exhibited a capacity of 135 mA h g^{-1} at 0.2C and 112 mA h g^{-1} at 30C. Even after cycling at 20C 1500 times, $NaVPO_4F$@C still showed a capacity retention of 90.4%, confirming its excellent long cycling stability. Furthermore, the symmetrical battery assembled with $NaVPO_4F$ could deliver a capacity of 82 mA h g^{-1} at 0.1C, which demonstrated the effective suppression of volume expansion. This excellent electrochemical performance was mainly due to the nanoscale feature of the $NaVPO_4F$ particles, which could shorten the diffusion distance of Na^+ and effectively accelerate the Na^+ diffusion in the electrode, and the suitable thickness of the carbon layer effectively accelerated the electron transfer.[101] In the study by Ge *et al.*, $NaVPO_4F$/C was synthesized *via* the solvothermal approach, where PVP was added to restrict the overgrowth of particles and a carbon source to generate a uniform carbon coating on $NaVPO_4F$. Benefiting from the enhanced electronic conductivity (4.2×10^{-2} S cm^{-1}), the obtained $NaVPO_4F$/C-PVP cathode showed an excellent electrochemical performance, delivering 111 mA h g^{-1} at 0.1C and maintaining 82% capacity retention over 1000 cycles at 10C.[102] Zhao *et al.* successfully synthesized $NaVPO_4F$ nanoparticles evenly embedded in an rGO network (Fig. 6a and b). The advantages of the nano-structure were described based on three aspects, as follows: (i) the uniform and robust rGO network inhibited the overgrowth and aggregation of $NaVPO_4F$ during calcination and buffered the volume changes of $NaVPO_4F$ during the sodiation/desodiation processes, which contributed to the outstanding cyclability; (ii) the $NaVPO_4F$ nanoparticles wrapped in the highly interconnected carbon network produced continuous short and ultrafast Na^+/e^- transport paths, improving the reaction kinetics in the $NaVPO_4F$ cathode; and (iii) the large connect area structure with abundant activated sites contributed to the infiltration of the electrolyte, accelerating the charge transfer at the interface. In addition, a full-cell composed of HC||NVPF@5% rGO was designed, exhibiting a superior rate performance (Fig. 6c) and long cyclability (Fig. 6d). For real application, a series of LEDs were lit by the full-cell and pouch cell.[99] Similarly, Cheng *et al.* designed nano-$NaVPO_4F$ enwrapped in rGO network. The rGO also constituted a 3D conductive network, and the $NaVPO_4F$ nanoparticles were

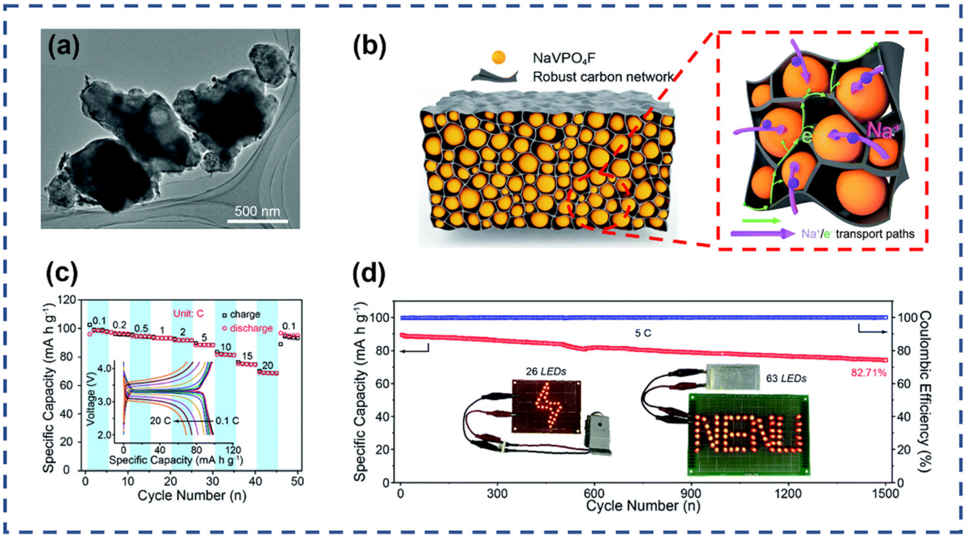

Fig. 6 (a) SEM of NaVPO$_4$F@rGO. (b) Schematic diagram of the structure of NaVPO$_4$F@rGO and corresponding transfer pathway of Na$^+$/e$^-$. (c) Rate performance of NaVPO$_4$F@rGO full cell (inset: GCD curves at different C-rates). (d) Cyclability of NaVPO$_4$F@rGO full cell (inset: LEDs lit by full cell and pouch cell). Reproduced with permission.[99] Copyright 2020, The Royal Society of Chemistry.

uniformly wrapped in the rGO sheets. The as-prepared NaVPO$_4$F exhibited an unexpected rate capacity, displaying a reversible capacity of 86.5 mA h g^{-1} even when cycled at 100C. This impressive electrochemical performance can be attributed to the nanometre-sized particles, which greatly shortened the diffusion pathway for Na$^+$ migration and the 3D conductive network accelerated the surface electron transfer.[103] Chen *et al.* synthesized NaVPO$_4$F/C *via* a facile carbon thermal method, which exhibited a high ion diffusion coefficient, acting as bipolar electrodes to assemble a full sodium-ion battery. When NaVPO$_4$F/C acted as the cathode in SIBs, it delivered a capacity of 123 mA h g^{-1} at 50 mA g^{-1} and 50 mA h g^{-1} at 2000 mA g^{-1}. The symmetric full battery assembled using NaVPO$_4$F/C had excellent compatibility, which effectively curbed the volume expansion. Consequently, the symmetric full battery exhibited an excellent rate storage of 42 mA h g^{-1} at 2000 mA g^{-1} and prolonged cyclability of 400 cycles at 50 mA g^{-1}, showing its potential for applications by lighting a series of LEDs.[104]

Elemental doping is also an effective method. In 2006, Zhuo *et al.* synthesized a monoclinic NaV$_{1-x}$Cr$_x$PO$_4$F (x = 0–0.1) material *via* a solid-state reaction. A small amount of Cr doping led to the enhanced cyclability of NaV$_{1-x}$Cr$_x$PO$_4$F, and the optimized NaV$_{1-x}$Cr$_x$PO$_4$F (x = 0.08) could deliver a great capacity retention of 91.4% after 20 cycles, surpassing the Cr-free sample. According to the FT-IR and XRD characterization, the Cr-doped samples showed decreased lattice parameters, while the crystallinity of the material increased, and thus the Cr-doped samples had better cyclic stability.[105] Unlike elemental doping, morphological regulation is frequently used to enhance the Na storage capability of the NaVPO$_4$F material. In the study by Jin *et al.*, a novel NaVPO$_4$F/C nanofibers self-supporting cathode was fabricated *via* electrospinning, and the 3D conductive network formed by the interconnection of NaVPO$_4$F/C nanofibers boosted the Na$^+$/e$^-$ transportation of NaVPO$_4$F and prevented the aggregation of the NaVPO$_4$F particles upon cycling. The NaVPO$_4$F/C cathode could deliver 126.3 mA h g^{-1} (1C) and exhibited an extraordinary rate capability of 61.2 mA h g^{-1} at 50C and excellent cyclability of 96.5% capacity retention over 1000 cycles at 2C. Furthermore, the as-assembled full cell (anode: NaTi$_2$(PO$_4$)$_3$) delivered an initial capacity of 80 mA h g^{-1}, which remained at 65.7 mA h g^{-1} after 50 cycles. Additionally, it successfully lit a 1.8 V LED, which confirmed its practical application potential.[100] Feng *et al.* prepared an NaVPO$_4$F/C cathode material *via* a facile sol–gel method. In the 3D coral-like structure (Fig. 7a–c), the NaVPO$_4$F nanoparticles were immobilized on the substrate *via* the effective hydrogen bonding between the fluorine ions and hydrogen atoms. Subsequently, coral-like structures with complete and regular hexagonal sheets were formed and the surface of the NVPF nanoparticles was uniformly covered with conductive carbon layers. The optimized NVPF-750-12 cathode exhibited an extraordinary rate capability with complete charge–discharge curves at a high rate (Fig. 7d), delivering 88 mA h g^{-1} even at 50C (Fig. 7e), excellent prolong cyclability, delivering 100 mA h g^{-1} at 5C and maintaining 70% capacity retention over 2500 cycles.[106]

Besides the above-mentioned studies on stoichiometric materials, non-stoichiometric Na$_{1+y}$VPO$_4$F$_{1+y}$ can be considered versatile electrodes for high-energy SIBs. For example, the reversible 116 mA h g^{-1} for y = 0.5, 103 mA h g^{-1} for y = 0.25 and 87 mA h g^{-1} for y = 0 were achieved. When y = 0.5, the material denoted as Na$_{1.5}$VPO$_4$F$_{1.5}$ with a tetragonal structure (*P*4$_2$/*mnm*) was formed. Besides, Young-Uk Park *et al.* synthesised a novel Na$_{1.5}$VPO$_{4.8}$F$_{0.7}$ material with high energy density of ∼600 W h kg^{-1}, which was derived from its multi-electron redox process (1.2 e$^-$ per formula unit) and working plateau (∼3.8 V *vs.* Na$^+$/Na) of the V$^{3.8+}$/V^{5+} redox couple. Furthermore, the Na$_{1.5}$VPO$_{4.8}$F$_{0.7}$ cathode showed outstanding cyclability

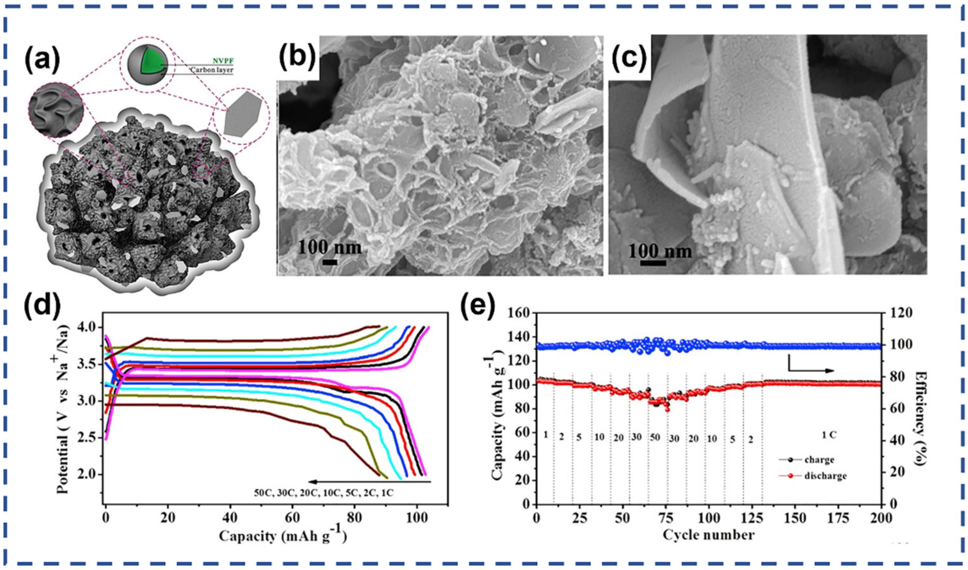

Fig. 7 (a) Schematical representation of porous 3D coral-like structured $NaVPO_4F/C$. (b and c) SEM of $NaVPO_4F/C$, (d) GCD curves and (e) rate performance of NVPF-750-12 at 5C. Reproduced with permission.[106] Copyright 2018, Elsevier.

(~84% capacity retention over 500 cycles). The excellent cyclability was mainly ascribed to the small volume change of 2.9% during cycling, which is the smallest volume change among the MVPF materials reported to date. Additionally, the abundant 2D Na^+ migration pathways led to low activation barriers for Na^+ diffusion, enabling an outstanding high-rate performance.[107]

3.1.2 $Na_3V_2(PO_4)_2F_3$. In the case of the $Na_3V_2(PO_4)_2F_3$ material produced from $Na_3V_2(PO_4)_3$, one $PO_4{}^{3-}$ was replaced by three F^-, and its high fluorine content gave it a strong induction effect and produced a high plateau (3.7 V and 4.2 V), thereby generating a high energy density of ~500 W h kg^{-1}. Nevertheless, due to its inherent poor electronic conductivity of approximately 10^{-12} S cm^{-1} owing to the separation of V atoms by $[PO_4]$ tetrahedra, it exhibited an unsatisfactory electrochemical performance.[63,76,108–111] Researchers frequently utilize the strategies of compositing with a conductive material, regulation of micro-nano structure and element doping to enhance the Na storage. Among them, the most favoured modification is compositing or packaging $Na_3V_2(PO_4)_2F_3$ with carbon to improve its electron conductivity, thus enhancing the electrochemical performance. Besides the common carbon materials, amorphous carbon, carbon quantum dots (CQD), N-doped carbon (NC), and three-dimensional graphene are also applied to increase the electronic conductivity, and finally enhance the electrochemical properties of $Na_3V_2(PO_4)_2F_3$.

N-doped carbon (NC) is one of the desirable carbon materials for the modification of NVPF due to its capability of providing additional active sites for Na^+ transfer, improving the surface wettability of the cathode materials and accelerating the charge transfer. Zhang *et al.* reported an NVPF/C-PDPA material in which the NC layer encapsulated on the surface was formed by the self-polymerization of DPA after calcination. The NVPF/C-PDPA cathode exhibited an outstanding rate performance (98 mA h g^{-1} at 10C) and cyclability (capacity retention of ~95.8% over 800 cycles) mainly benefiting from its homogeneous NC layer, which effectively protected the electrode material from corrosion and ensured the material integrity. In addition, the nitrogen doped in the centre of the carbon layer unsurprisingly provided abundant active sites, which enhanced the Na storage, and finally the rate performance.[112] Recently, a $Na_3V_2(PO_4)_2F_3$@NC subglobose was prepared using CTAB and PVDF as the carbon source. The CTAB not only acted as a soft template but also increased the conductivity of the carbon layer as $-(CH_3)_3N^+$ in CTAB was combined with the residual carbon from PVDF to form partially N-doped carbon. Consequently, the optimised NVPF cathode a showed high initial capacity of 121.5 mA h g^{-1} at 0.1C and high capacity retention of 90.1% over 1000 cycles at 10C.[113] Likewise, the C@$Na_3V_2(PO_4)_2F_3$-assembled half-cell exhibited a superior rate capability (72 mA h g^{-1} at 10C) and great cyclability (remaining 85% capacity retention for 200 cycles), which benefitted from the nanosized spherical and porous particles formed by the addition of CTAB in a certain amount.[114] Besides, Wang *et al.* innovatively designed an N-doped carbon nanotube decorated $Na_3V_2(PO_4)_2F_3$ material, in which the N-doped carbon nanotubes could not only accelerate the charge transfer but also reduce the polarization of the electrode material, and the huge specific surface area of the CNTs contributed to the excellent pseudo-capacitance effect for Na storage. Finally, the electrochemical characteristics of the N-doped carbon nanotube-decorated NVPF particles were significantly enhanced, exhibiting a capacity of 126 mA h g^{-1} at 0.5C and 76 mA h g^{-1} at an ultrahigh-rate of 100C, showing a unique high-rate Na^+ storage capacity. Besides, it maintained 60.4% capacity retention after 1500 cycles at 40C.[115] Gu *et al.* researched the introduction of carbon in NVPF materials in-depth, where the NVPF particles were covered with a uniform carbon shell of approx. 5–6 nm thickness. The newly generated C=O, P–C, and V–F–C bonds, as shown in the high-resolution P 2p, O 1s, and F 1s spectra, confirmed the tight binding of carbon to the NVPF substrates (Fig. 8a). Among them, the presence of V–F–C bonds were shown to have an effect of increasing the working voltage. Consequently, as shown in Fig. 8b, the voltage plateau of NVPF@C was significantly higher than that of p-NVPF, and it exhibited a high rate capacity (Fig. 8c). According to the results of the apparent Na^+ diffusion coefficient calculated by GITT, NVPF@C (1.6×10^{-11} cm^2 S^{-1}) was significantly better than p-NVPF (9.9×10^{-12} cm^2 S^{-1}), which was obviously due to the tight binding of NVPF and C to accelerate the diffusion kinetics. The high reversibility of the NVPF@C was shown by the evolution of the (220), (113), (222) and (213) peaks during the charging and discharging process *via in situ* XRD and the mechanism was consistent with the $Na_3V_2(PO_4)_2F_3 \leftrightarrow NaV_2(PO_4)_2F_3$ (Fig. 8d). To explore its potential applications, the NVPF-based material as a cathode was coupled with the HCC anode. Consequently, HCC‖NVPF@C exhibited a remarkable rate tolerance of 88 mA h g^{-1} even at 20C, maintaining 99.7 mA h g^{-1} over 200 cycles at 0.5C, which surpassed the p-NVPF electrode.[63]

The construction of a nano-micro morphology is also applicable to enhance the properties of NVPF materials. Recently, Zhu *et al.* used the method of regulating the grain growth direction through the addition of inorganic NaCl. The quantitative addition of NaCl induced the growth of NVPF crystal gains along the [110] direction, leading to the formation of a large (001) surface, enabling the distribution of more Na^+. Besides, large tunnels along the $[1\bar{1}0]$ and [110] planes were formed and provided fast pathways for Na^+ diffusion. The optimised NVPF@rGO cathode displayed a great capacity of 127.5 mA h g^{-1} at 0.2C, remarkable rate capability of 73.7 mA h g^{-1} at a high rate of 50C and great cyclability, maintaining 83% capacity retention over 1000 cycles at 5C. Impressively, the full batteries fabricated using the NVPF cathode and CSC anode demonstrated 108 mA h g^{-1} at 0.5C and stable operation at 5C for up to 500 cycles.[116] In addition to the above-mentioned treatment in maintaining the original rectangular shape of NVPF on the regulation of crystal surface growth, researchers also constructed a variety of special nano-micron morphologies such as microcubes, nanofibers, hollow spheres, and flower shapes to create more transfer paths and optimize the stability of electrodes. Li *et al.* prepared a fibre-like $Na_3V_2(PO_4)_2F_3$@NC for SIBs *via* simple electrostatic spinning, which showed a superior Na storage performance including excellent rate tolerance of 78.9 mA h g^{-1} at 30C and gratifying long-term cyclability (83.4% capacity retention after 1500 cycles at 50C). Besides, full batteries with a high energy density of 357.3 W h kg^{-1} and capacity retention of 82.4% over 150 cycles at 1C could be achieved when coupling the $Na_3V_2(PO_4)_2F_3$@C cathode with a hard carbon anode. This enhanced performance was attributed to the fast Na-ion/electron transport network composed of intertwined N-doped carbon fibers.[117] Liu *et al.* prepared a $Na_3V_2(PO_4)_2F_3$@C nano-compound with a core/double shell-like structure (denoted as $Na_3V_2(PO_4)_2F_3$@C_D) *via* a simple sol–gel method, followed by calcination, and the $Na_3V_2(PO_4)_2F_3$ nanoparticles with a uniform carbon coating were embedded in an ordered mesoporous carbon framework (Fig. 9a). The as-synthesis $Na_3V_2(PO_4)_2F_3$@C_D compound exhibited high-rate tolerance and superior cycling performance, displaying a capacity of 63 mA h g^{-1} even when tested at 100C, and a prolonged lifespan of 5000 cycles at 50C could be

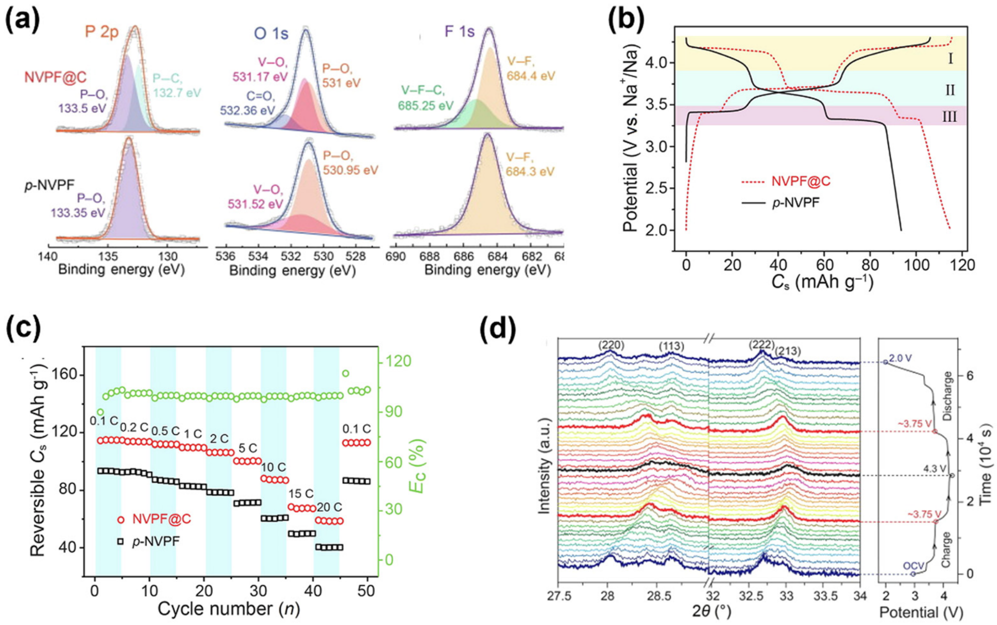

Fig. 8 (a) High-resolution XPS spectra and corresponding deconvolution results for the peaks of P 2p, O 1s, and F 1s, (b) GCD curves at 0.1C, (c) rate performance and (d) partly enlarged *in situ* XRD patterns in the 2θ range of 27.5°–34° with the corresponding GCD curve. Reproduced with permission.[63] Copyright 2020, Elsevier.

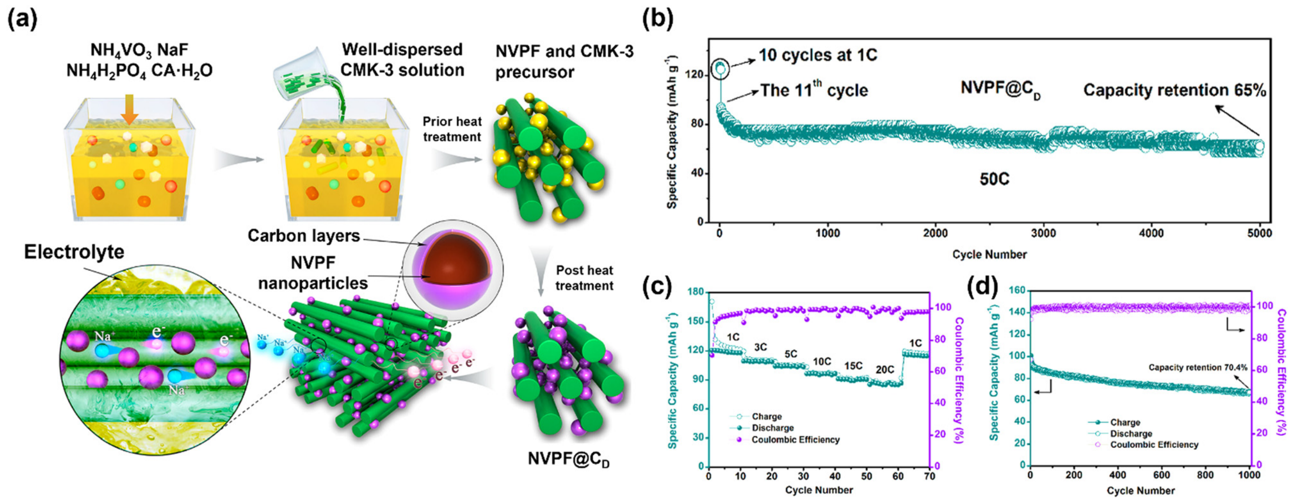

Fig. 9 (a) Schematical representation of the preparation of NVPF@C$_D$ compound and (b) cycling performance of NVPF@C$_D$ at 50C. (c) Rate performance and (d) cycle performance of NVPF@C$_D$||NaTi$_2$(PO$_4$)$_3$@C full batteries. Reproduced with permission.[118] Copyright 2016, the American Chemical Society.

achieved. These results are attributed to the fully exposed electrochemical reaction surface and ample paths for Na$^+$/e$^-$ migration (Fig. 9b). Moreover, the assembled $Na_3V_2(PO_4)_2F_3$@C$_D$||NaTi$_2$(PO$_4$)$_3$@C full batteries also showed an impressive rate capacity of 85 mA h g^{-1} at 20C (Fig. 9c), maintaining 71% capacity retention over 1000 cycles when cycled at 10C (Fig. 9d), confirming the potential application of the $Na_3V_2(PO_4)_2F_3$@C$_D$ material.[118] Liu *et al.* applied carbon quantum dots (CQDs) to modified $Na_3V_2(PO_4)_2F_3$, and the as-prepared NVPF@CQD composite exhibited an excellent rate performance, delivering 105.1 mA h g^{-1} at 20C and maintaining 90.2% capacity retention over 6000 ultra-long cycles when cycled at 30C, displaying superior long-term cyclability. To confirm its practical application, an NVPF@CQDs||HC full-cell was assembled, which exhibited a high working plateau (~3.0 V) and excellent cyclability (82.8 mA h g^{-1} for 400 cycles at 0.05 A g^{-1}). The main role of the carbon quantum dots was to induce the self-assembly of NVPF into microsphere structures and boost the electron transfer in the NVPF cathode.[119]

As one of the effective strategies, heteroatomic doping has also attracted significant attention from researchers. Numerous cations can be applied in process of element doping in NVPF, varying from monovalent (K$^+$ and Li$^+$) and divalent (Mg^{2+} and Mn^{2+}) cations to trivalent cations (Cr^{3+}, Ti^{3+}, Al^{3+}, and Y^{3+}). In this case, doping these elements in NVPF-type materials can considerably enhance their Na$^+$ storage capability.[120–130] According to the substitution sites, the cation doping can be divided into two classic types, *i.e.*, Na sites and V sites. The ions doped in the Na site mainly include Li$^+$ and K$^+$. The introduction of the larger ionic radius K$^+$ in the Na site can expand the lattice spacing, proving more channels for Na$^+$ transfer. In Li's work, K$^+$ was partially introduced in the Na sites and the special NKVPF@CNT material was obtained *via* the sol–gel method. Based on the fitting and calculated results of CV at different scan rates, the Na$^+$ diffusion coefficient in the K$^+$-doped compound ($1 \sim 3 \times 10^{-11}$ cm^2 s^{-1}) was at least 2–3 times greater than that of the K-free sample. This rapid diffusion of Na$^+$ led to a great capacity of 120 mA h g^{-1} at 1C and a capacity retention of 90% was maintained over 6000 cycles at 50C (Fig. 10a), demonstrating enhanced cyclability and high current tolerance.[125] Kosova *et al.* successfully synthesized a mixed $Na_{3-x}Li_xV_2(PO_4)_2F_3$ composite with a tetragonal structure *via* the solid-state method, and subsequently electrochemical Na$^+$/Li$^+$ exchange. The prepared $Na_{3-x}Li_xV_2(PO_4)_2F_3$ had an excellent enhanced performance, which is partly due to the pseudocapacitance effect caused by the smart design of the material, including the *in situ* mixed coating of submicron particles, conducting carbon and V_2O_3. Consequently, the optimized Li-doped $Na_{2.93}Li_{0.07}V_2(PO_4)_2F_3$ sample showed a superior rate capacity, delivering 100 mA h g^{-1} at 10C and 80 mA h g^{-1} at a high rate of 20C, which surpassed that the Li-free sample. Compared with the pristine NVPF, the synergistic effect of surface coating increased the conductivity of the multicomponent Na/Li cathode material by 4 orders of magnitude, significantly reduced the activation energy of the conductivity, and improved the rate capability of the multicomponent material in the SIBs (Fig. 10b).[131] The elements that could be substituted at the V-site were divided into two categories, *i.e.*, electrochemically active and non-electrochemically active. The elements with electrochemical activity mainly include Ti, Cr, Zr, and Mn. The effects of the substitution of various titanium (Ti) ions on the electronic conductivity and ion transport rate of the $Na_3V_{2-x}Ti_x(PO_4)_2F_3$ materials were explored in this regard through the two strategies of doping elements with the same valence state and changing the valence state. The optimized material could exhibited 125 mA h g^{-1} at 0.2C and 104 mA h g^{-1} at 40C (Fig. 10c).[132] Guo *et al.* reported the preparation of a Zr-doped NVPF composite wrapped with a thin NC layer *via* a facile sol–gel method. The optimized Zr-doped NVPF/NC cathode delivered a high reversible capacity of 119.2 mA h g^{-1} at 0.5C, exhibiting a remarkable rate performance and superior cyclability for 1000 cycles at 20C (Fig. 10d).[127]

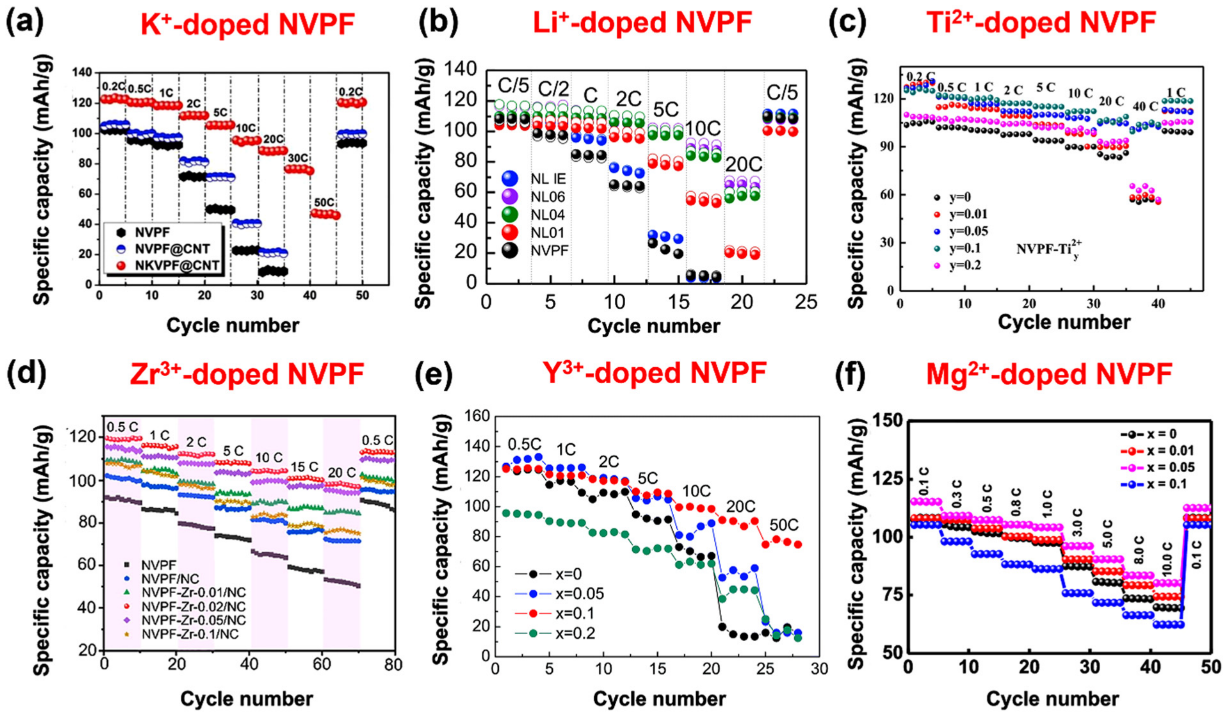

Fig. 10 Rate capacities of (a) K^+-doped NVPF-based materials (reproduced with permission.[125] Copyright 2019, Elsevier), (b) Li^+-doped NVPF ($0 \leq x \leq 0.06$) (reproduced with permission.[131] Copyright 2018, Elsevier), (c) Ti^{2+}-doped NVPF ($0 \leq y \leq 0.2$) (reproduced with permission.[132] Copyright 2018, Elsevier), (d) Zr^{3+}-doped NVPF/NC ($0 \leq x \leq 0.1$) (reproduced with permission.[127] Copyright 2022, Elsevier), (e) Y^{3+}-doped NVPF ($0 \leq x \leq 0.2$) (reproduced with permission.[128] Copyright 2017, Elsevier), and (f) Mg^{2+}-doped NVPF ($0 \leq x \leq 0.1$) (reproduced with permission.[122] Copyright 2021, the American Chemical Society).

The above-mentioned modifications confirmed that the *ex situ* substitution of electrochemically active elements contributed significantly to the enhancement of the electrochemical performance. Besides, non-active elements have been proven to exhibit certain merits such as providing extra channels for Na^+ transfer and stabilizing the crystal structure during desodiation/sodiation. Liu *et al.* proposed the doping of the rare earth element yttrium (Y) in NVPF to improve its intrinsic conductivity, achieving the discharge capacity of 121.3 mA h g^{-1} at 0.5C. Moreover, excellent rate storage was demonstrated, delivering 80 mA h g^{-1} even at 50C (Fig. 10e). The enhancement in electrochemical properties was mainly due to the intrinsic electron conductivity and Na^+ mobility caused by the introduction of an appropriate amount of Y instead of V-site in the crystal structure of NVPF; the creation of a relatively weak Y–O bond between Y and O during the insertion of Y^{3+} into the V site; the Y–O bond accelerated the electron transport in NVPF; and the embedded Y^{3+} expanded the lattice spacing of NVPF and created a larger Na transport channel.[128] Puspitasari *et al.* successfully doped Mg^{2+} in the V site of NVPF materials *via* the sol–gel method and investigated the effect of a low Mg concentration (x = 0, 0.01, 0.05, and 0.1) on the NVPF lattice and its electrochemical properties. The optimized $Na_3V_{1.95}Mg_{0.05}(PO_4)_2F_3$/C cathode with the highest electron conductivity ($\sim$1.4 × 10^{-5} S cm^{-1}) showed an enhanced rate performance, exhibiting a high initial capacity of 80 mA h g^{-1} at 10C with 88% capacity retention over 500 cycles (Fig. 10f). The XRD results demonstrated that the appropriate Mg doping amount could reduce the crystal grain and particle size. Moreover, the substitution of Mg^{2+} in the vanadium site also enhanced the electron/ion conduction and acted as a pillar to enhance the structural stability of the NVPF material.[122]

3.1.3 $Na_3V_2O_2(PO_4)_2F$.

The $Na_3V_2O_2(PO_4)_2F$ material exhibits a high theoretical capacity (130 mA h g^{-1}) and high average operating plateau ($\sim$3.8 V), making it competitive for realizing high-energy SIBs. However, this material also suffers from sluggish migration kinetics due to its low electronic conductivity ($\sim$1.8 × 10^{-7} S cm^{-1}).[83,133–138] Hence, it is necessary to enhance the properties of $Na_3V_2O_2(PO_4)_2F$ by proper modification. Carbon coating has proven to be a facile and feasible modification for $Na_3V_2O_2(PO_4)_2F$ material. Recently, Shen *et al.* reported the preparation of an NVPOF/KB material *via* a simple one-step high-energy ball-milling method (Fig. 11a). The as-prepared nanoscale NVPOF exhibited good crystallinity with a clear lattice spacing of 0.4425 nm, corresponding to the (110) plane from NVPOF. After coating with Ketjenblack (KB), the NVPOF/KB cathode showed a high rate capacity and impressive long-term cyclability of 98% capacity retention over 10 000 ultra-long cycles at 20C (Fig. 11b). The outstanding rate capacity and cyclability benefited from the nano-crystallization and extra active sites for Na^+ storage, and the highly conductive KB coating enhanced the charge transfer on the material surface. Toward practical large-scale application, a 26650-type sodium ion battery was assembled with an HC anode, which showed an impressive rate performance, displaying 1329 mA h

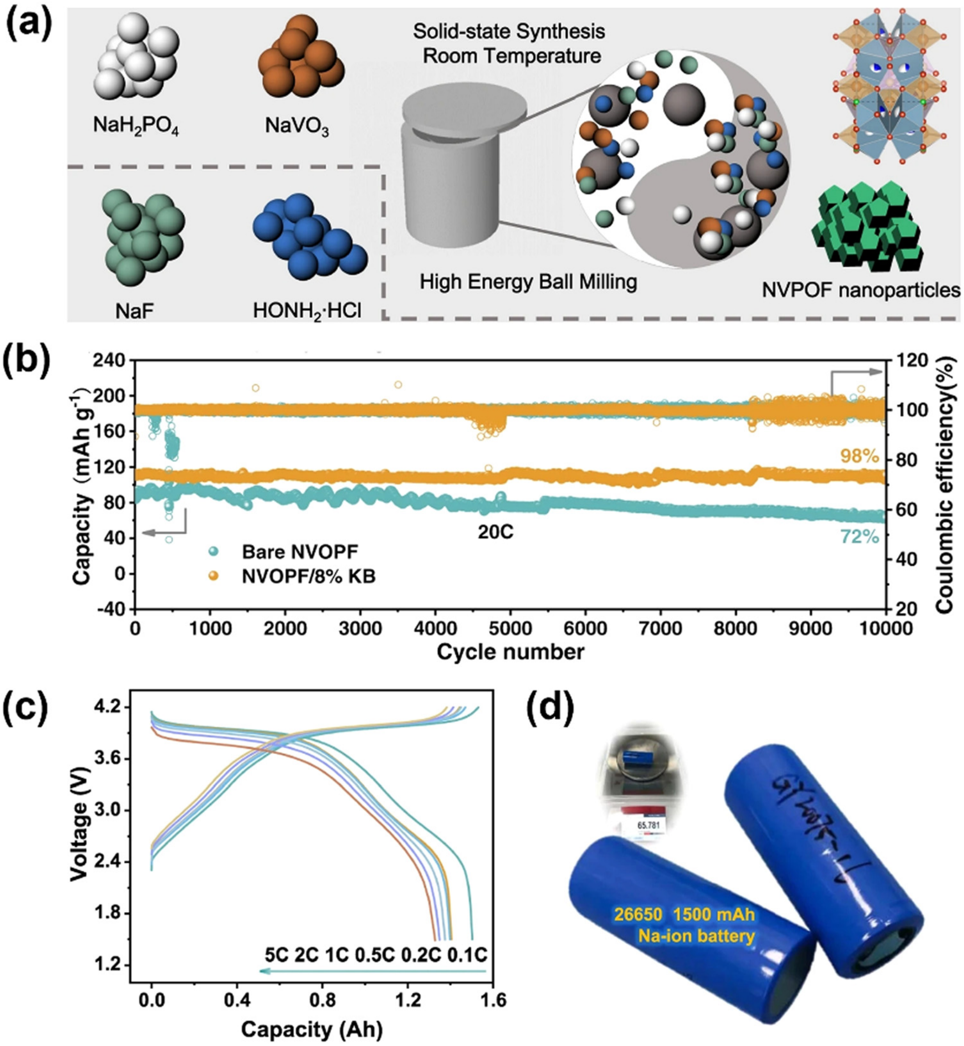

Fig. 11 (a) Schematical representation of fabrication of NVPOF@KB. (b) Long cyclability of NVPOF-based materials at 20C. (c) Rate performance and (d) digital image of 26550-type Na-ion batteries. Reproduced with permission.[134] Copyright 2021, Springer.

at 5C (Fig. 11c) and cyclability of 94.5% capacity retention over 100 cycles at 3C, greatly demonstrating its practical application value (Fig. 11d).[134] Zhang *et al.* proposed the use of NVPOF microspheres coated with N/P dual-ion-doped carbon as a promising cathode for SIBs. The N/P-doped carbon was tightly fitted on NVPOF due to the bridging effect of P, showing a great protective effect, which hindered the occurrence of side effects. According to DFT calculations, the N/P dual-doped carbon layer could greatly enhance Na^+/e^- migration mobility due to the lower Na^+ migration energy barrier. The as-prepared NVPOF@P/N/C cathode showed a great discharge capacity of 128 mA h g^{-1} at 0.5C and 122 mA h g^{-1} at 2C. Besides, it demonstrated cycling stability of 99.4 mA h g^{-1} after 500 cycles at 2C.[139] Li *et al.* reported the preparation of a double-layer carbon decorated $Na_3V_2O_2(PO_4)_2F$ *via* a simple solvothermal method. The $Na_3V_2O_2(PO_4)_2F$@C/CNF cathode showed an impressive rate storage of 86.7 mA h g^{-1} at 50C and long lifespan with 82.5% capacity retention after 2500 cycles at 5C. This excellent performance was also observed at 60 °C, proving the excellent thermal stability of the amorphous carbon and graphitized carbon nanofiber-coated NVPOF cathode.[140] Besides the above-mentioned use of carbon as a coating medium, conductive metals and their oxides often perform well as a coating layer for $Na_3V_2O_2(PO_4)_2F$ materials. In a pioneering study, Xia *et al.* employed ruthenium (Ru) metal and its oxides as a conductive coating for improving the intrinsic conductivity of $Na_3V_2O_2(PO_4)_2F$. Novel hierarchical Ru-doped $Na_3V_2O_2(PO_4)_2F$ hollow microspheres were fabricated *via* a facile solvothermal reaction, and a high specific capacity of 103 mA h g^{-1} and 45 mA h g^{-1} were achieved at high rates of 20C and 100C, respectively with the support of the highly conductive RuO_2 layer.[141] Besides, they also prepared RuO_2-coated $Na_3V_2O_2(PO_4)_2F$ nanowires *via* hydrothermal synthesis regulated by extra microemulsion. Due to the advantages of the highly conductive RuO_2 layer and its nanostructure, the RuO_2-coated $Na_3V_2O_2(PO_4)_2F$ nanowires exhibited an excellent rate capacity, delivering 80 mA h g^{-1} over 1000 cycles even at 20C.[142] Du *et al.* synthesized titanium dioxide layer with oxygen defect

(TiO_{2-x})-coated $Na_3V_2O_2(PO_4)_2F$ nanosheets (NVOPF@TiO_{2-x}) *via* the hydrothermal approach. The NVOPF@TiO_{2-x} cathode showed 105 mA h g^{-1} (0.2C) after 100 cycles, retaining 54 mA h g^{-1} after 500 cycles at 1C, showing enhanced cycling capability. In summary, the enhanced performance was attributed to the following aspects: the TiO_{2-x} layer could separate NVPOF from the electrolyte to avoid their direct contact, which efficiently inhibited extra side reactions causing the micro-dissolution of vanadium and diminishing the charge transfer resistance during cycling; moreover, the oxygen-deprivation in TiO_{2-x} layer provided adequate ion-storable sites, which effectively increased the Na^+ diffusion coefficient at the interface. Multiple synergistic effects effectively enhanced the electrochemical properties of the NVOPF cathode, demonstrating that conductive metal–oxide coating is an efficient strategy for its modification.[143]

Morphological regulation is another common method to improve the properties of NVPOF. Lately, Zheng *et al.* proposed an interesting microfluidics-based continuous-flow strategy for the fabrication of $Na_3V_2O_2(PO_4)_2F$ with different nanomorphologies (nanospheres and nanosheets). NVPOF presented different morphologies by changing the amount of H^+, which induced crystal growth in NVPOF. Spherical (Fig. 12b), platelike (Fig. 12c) and rodlike (Fig. 12d) crystals were formed at the pH values of 5.7, 3.6 and 1.3, respectively. The nanospheres obtained by ultra-fast synthesis (6.3 s) showed a rate capacity of 114 mA h g^{-1} at 10C (Fig. 12e), while the nanosheets exhibited 106.1 mA h g^{-1} at 10C (Fig. 12f) and the capacity retention of 97.3% after 1000 cycles (Fig. 12g), which particularly could maintain 81.5% capacity retention over 3000 cycles (Fig. 12h).[144] Qi *et al.* presented a rapid and convenient strategy for the fabrication of multi-shelled hollow NVPOF microspheres under room temperature conditions combined with liquid–liquid extraction-separation and material synthesis. The bubbles generated from $HONH_2$ acted as a soft template, and the interaction between the static electricity carried by the bubbles and the nanoparticles could make the nanoparticles aggregate on the surface of the bubbles. The aggregation of the nanoparticles eventually resulted in the formation of a shell, on which more bubbles were generated *in situ*, repeating until a multilayer hollow shell was formed. The special multi-shelled hollow microsphere structure could offer a large contact area, which generated more active sites and provided fast pathways for Na^+/e^- migration without extra carbon-coating. Finally, the as-synthesized NVPOF cathode exhibited a remarkable Na-storage performance, demonstrating 98.6 mA h g^{-1} at 10C and excellent cycle performance of 70% capacity retention over 3000 cycles at 15C.[145] Zhao *et al.* proposed the preparation of $Na_3V_2(PO_4)_2O_2F$ hollow nanospheres (denoted as NVPF-hs) *via* a one-step template-free method, which demonstrated an unexpected rate capability of 85.4 mA h g^{-1} at 50C and long lifespan of 2000 cycles at 20C. The SEM and TEM results revealed that an individual nanosphere was assembled by numerous nanoparticles, and this special conformation significantly shortened the distance for Na^+ transfer and facilitated Na^+ migration. The characteristics of the hollow and hierarchically porous structure enabled full penetration of the electrolyte, ensuring continuous electrolyte replenishment and easy electrolyte delivery, and the large specific surface area also effectively boosted the charge transfer throughout the electrode, leading to rapid Na^+/e^- diffusion, and thereby enhanced high-rate capability and long-term cyclability.[146]

Currently, the heteroatomic doping strategy for NVPOF materials has also been reported, mainly focusing on doping the vanadium and polyanion sites. In terms of V-site doping, Yue and co-worker explored the influence of different Fe doping amounts on the properties of NVPOF. The optimized $Na_3V_{1.85}Fe_{0.15}(PO_4)_2O_2F$ (NVFPOF) cathode displayed 137 mA h g^{-1} at 1C (exceeding the theoretical capacity of NVPOF) and maintained 98.5% capacity retention after 100 cycles with the CE of

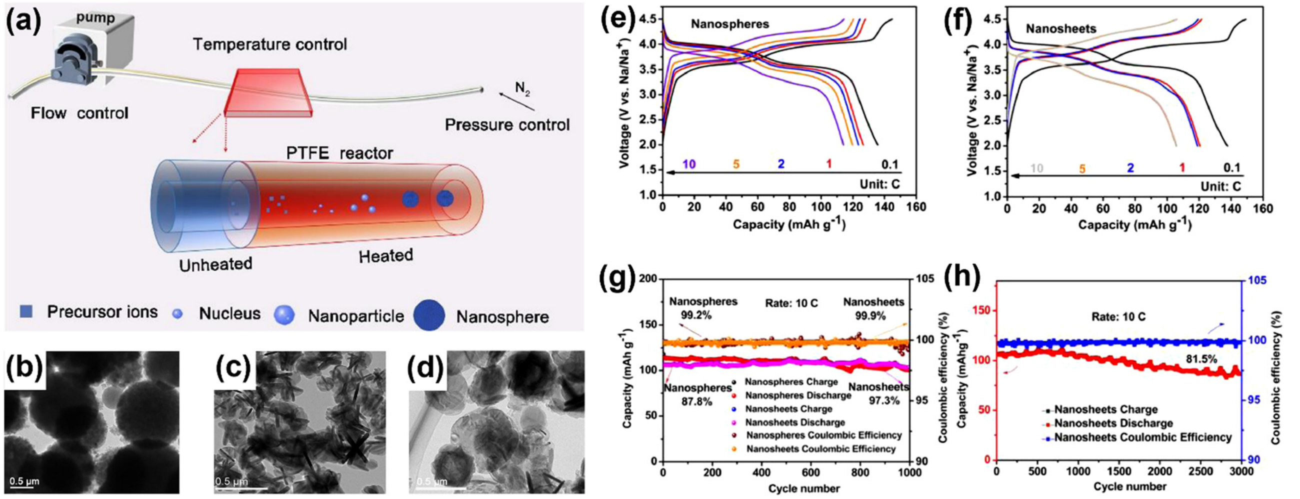

Fig. 12 (a) Schematic representation of rapid preparation of NVPOF materials. (b) Spherical, (c) plate-like and (d) rod-like NVPOF at different pH values. GCD curves at different rates of (e) NVPOF nanospheres and (f) NVPOF nanosheets. (g) Cycling performance of NVPOF nanospheres and NVPOF nanosheets. (h) Long-term cycling performance of NVPOF nanosheets. Reproduced with permission.[144] Copyright 2021, Elsevier.

100%. Even when cycled at 20C, the NVFPOF half-cell maintained a capacity retention of 86% after 1000 cycles, exhibiting the outstanding cyclability of the electrode. Furthermore, the assembled $Na_3V_{1.85}Fe_{0.15}(PO_4)_2O_2F$||HC full cell also exhibited excellent practical application by displaying 102 mA h g^{-1} and maintaining 82.3% capacity retention over 100 cycles at 0.4C. The Fe-substitution could shorten the length of the V–O bond, and Fe^{3+} acted as a pillar to stabilize the host structure and buffer the volumetric strain generated from repeated Na^+ (de)insertion. Furthermore, the disordered arrangement between the $[VO_5F]$ octahedron and $[PO_4]$ tetrahedron was alleviated. Thus, the potential lattice collapse during the reversible sodiation/desodiation process was prevented, which inhibited the adverse phase transition, and then improved the stability of the host structure, revealing the fundamental reason for the outstanding cyclic performance of the Fe-substituted material.[147] Wang *et al.* successfully introduced the heterophase dopant Cl in NVPOF *via* the facile chemical vapor replacement method. As shown in Fig. 13a and b, the DFT calculation demonstrated that the local electron density and structure in the NVPOF lattice were tuned after Cr substitution, leading to the redistribution of electrons between the vanadium centre and dangling anions, which effectively improved the Na^+ migration kinetics and reduced the interfacial transfer

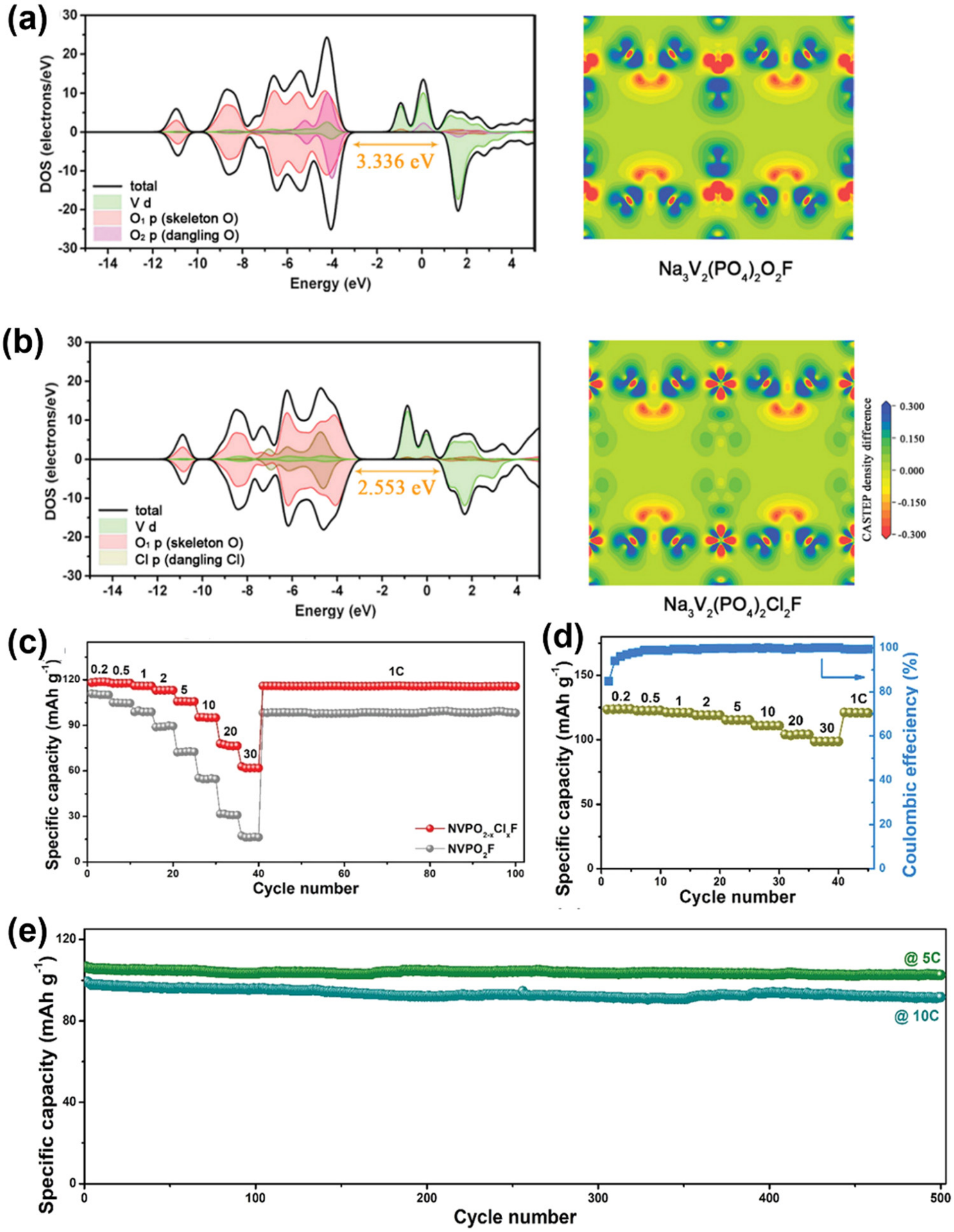

Fig. 13 Density of states (DOS) and sliced iso-surface of (110) plane of (a) $Na_3V_2(PO_4)_2O_2F$ and (b) $Na_3V_2(PO_4)_2Cl_2F$. (c) Rate comparison of NVPOF-based cathode. (d) Rate capacity and (e) cycling performance of $NVPO_{2-x}Cl_xF$||3DC@Se full batteries. Reproduced with permission.[148] Copyright 2021, Wiley-VCH.

resistance. The as-synthesized NVPO$_{2-x}$Cl$_x$F cathode materials exhibited a great rate capability of 63 mA h g^{-1} at 30C (Fig. 13c) and prolonged cycling stability of 1000 cycles at 10C; moreover, 314 W h kg^{-1} at a high power density of 5850 W kg^{-1} and cycling stability (capacity retention of 96.3% after 500 cycles at 5C and 92.4% over 500 cycles at 10C) were obtained for the NVPO$_{2-x}$Cl$_x$F||3DC@Se full batteries, demonstrating their extraordinary potential for practical applications (Fig. 13d and e).[148]

3.1.4 $Na_3V_2O_{2-2x}(PO_4)_2F_{1+2x}$ ($0 < x < 1$). $Na_3V_2O_{2-2x}(PO_4)_2F_{1+2x}$ ($0 < x < 1$) cathode materials are particularly fascinating due to their high theoretical capacity (128–130 mA h g^{-1}), high operating voltage (3.8–3.9 V *vs.* Na/Na$^+$) and great structural stability (<2% volume expansion), and thus it is worth exploring their application in SIBs. Similarly, coating with conductive materials, size and morphology regulation and element doping are proven to be effective modification strategies for NVPOF cathodes. For instant, P. Ramesh Kumar *et al.* studied the effects of multiple carbon materials (rGO, MWCNTs and Super P) on the particle size and electrochemical performance of $Na_3V_2O_{2x}(PO_4)_2F_{3-2x}$ cathodes. The composite with MWCNT as the carbon matrix obtained the minimum grain size for the $Na_3V_2O_{2x}(PO_4)_2F_{3-2x}$ cathode, exhibiting enhanced electrochemical properties of 98 mA h g^{-1} at 0.1C. Impressively, the full cell assembled with the NTP-MWCNT anode exhibited 98 mA h g^{-1} at 0.2C, surpassing the capacity of the $Na_3V_2O_{2x}(PO_4)_2F_{3-2x}$-rGO cathode (40 mA h g^{-1}) and $Na_3V_2O_{2x}(PO_4)_2F_{3-2x}$-SP cathode (51 mA h g^{-1}).[149] The same group also explored the electrochemical performance by controlling the proportion of $Na_3V_2O_{2x}(PO_4)_2F_{3-2x}$–rGO, which was synthesized *via* the hydrothermal method using CMC-Na binder. Notably, the surface coating of rGO improved the electronic conductivity of $Na_3V_2O_{2x}(PO_4)_2F_{3-2x}$, and the CMC-Na binder ensured efficient electronic transmission by maintaining the completeness of the electrodes during cycling. These synergistic effects significantly enhanced the electrochemical kinetics of the cathode. Concretely, the $Na_3V_2O_{2x}(PO_4)_2F_{3-2x}$–rGO cathode delivered 108 mA h g^{-1} at 0.1C and 98% capacity retention after 250 cycles.[150]

Specific stoichiometric $Na_3V_2O_{2-2x}(PO_4)_2F_{1+2x}$ ($0 < x < 1$) materials have also been reported. For instance, Partheeban *et al.* presented an innovative $Na_3V_2(PO_4)_2F_{2.5}O_{0.5}$ and its Li-substitution materials, which were fabricated *via* the solid-state flux method. The as-prepared $Na_3V_2(PO_4)_2F_{2.5}O_{0.5}$ and $Na_{2.4}Li_{0.6}V_2(PO_4)_2F_{2.5}O_{0.5}$ cathodes provided high discharge capacities of 107 and 110 mA h g^{-1} for SIBs at 0.1C, and maintained 72.7% and 80.4% of their initial capacity after 200 cycles, respectively.[151] Besides, a novel material of $Na_3(VO_{0.5})_2(PO_4)_2F_2$ embedded in a porous graphene framework was proven to be a high-quality cathode for SIBs by Xiang and coworkers, which displayed 100 mA h g^{-1} at 1C and maintained 73% capacity retention over 1000 cycles at an ultra-high rate of 50C. In addition, it is crucial that this work uncovered the importance of the effect of pseudo-capacitance behavior in the NVPF cathode for the construction of high-rate SIBs.[152] $Na_3V_2(PO_4)_2O_{1.6}F_{1.4}$ with the space group of $P4_2/mnm$ could deliver a high specific capacity of 156 mA h g^{-1}, corresponding to 2.4 e$^-$ per formula unit involved in electrochemical conversion when used in SIBs. In Palomares's work, the electrochemical properties and structural evolution of the $Na_3V_2O_{1.6}(PO_4)_2F_{1.4}$ cathode in SIBs were detailed studied. It was found that the flexible V$^{+3.8}$-based $Na_3V_2(PO_4)_2O_{1.6}F_{1.4}$ could extract sodium adequately based on its ability to withstand high voltage (4.8 V).[153] Similarly, Li and coworker prepared nano-structured $Na_3V_2(PO_4)_2O_{1.6}F_{1.4}$ *via* a facile microwave-assisted solvothermal method, which delivered 67 mA h g^{-1} even at 30C and maintained 61 mA h g^{-1} over 1000 cycles at 10C, demonstrating high rate tolerance and excellent cyclability due to the enhanced Na$^+$ migration kinetics.[153]

3.2 Potassium vanadium fluorophosphates

3.2.1 KVPO$_4$F. The KVPO$_4$F material, which is known for its high operating plateau (~4.0 V), is an advanced alternative for high-energy PIBs; however, its practical application is hindered by its poor intrinsic electronic conductivity and structural breakage or worse collapse during repeated K$^+$ insertion/extraction. Similar to the modification strategy of sodium vanadium fluorophosphates used in SIBs, surface coating and morphology control are also applicable to overcome the intrinsic low electronic conductivity of KVPO$_4$F. Additionally, its structural instability is relatively sophisticated and insurmountable on account of the larger K$^+$ easily causing structural collapse during potassiation/depotassiation. Thus, a robust protective layer or architecture needs to be constructed.[33,34,154] Xu *et al.* employed a facile multi-process to prepare a KVPO$_4$F/rGO composite, which exhibited a high working voltage of up to 4.22 V when used as a cathode in PIBs. On the one hand, the surface-coated rGO could sufficiently inhibit the aggregation of the KVPO$_4$F particles; on the other hand, it enhanced the e$^-$/K$^+$ diffusion kinetics. The as-obtained KVPO$_4$F/rGO manifested 103.2 mA h g^{-1} and corresponding high energy density of 436.5 W h kg^{-1}; moreover, the superior rate storage of 88.1 mA h g^{-1} at 50C and cyclability of 76.9% were maintained after 500 cycles under 10C. Besides, the KVPO$_4$F/rGO||PSC full cell assembled with the synthesized KVPO$_4$F/rGO cathode and pitch-derived soft carbon (PSC) anode also had a superior electrochemical performance, showing a high reversable capacity of 105 mA h g^{-1} at 50 mA g^{-1} and 73.4 mA h g^{-1} at 2000 mA g^{-1}.[155] Liao *et al.* prepared a KVPF@C composite generated from flower-like VPO$_4$ in which the particles were trapped in a carbon framework. As shown in Fig. 14a and b, the KVPF@C cathode exhibited the special high initial capacity of 103 mA h g^{-1} at 20 mA g^{-1}, exceptional rate performance of 87.6 mA h g^{-1} at 5 A g^{-1} and long cyclability of 900 cycles at 1 A g^{-1}. Moreover, when coupled with a VPO$_4$ anode (Fig. 14c), the assembled KVPF@C||VPO$_4$ full batteries demonstrated high discharge rate tolerance (50C, Fig. 14d) and possessed a long lifespan of 2000 cycles with a capacity retention of 86% (Fig. 14e), displaying great practical applicability.[156] He *et al.* successfully synthesized an excellent multi-component coated KVPO$_4$F cathode material with attractive electrochemical performance, and the corresponding full batteries possessed a high energy density of up to 337 W h kg^{-1} and enhanced

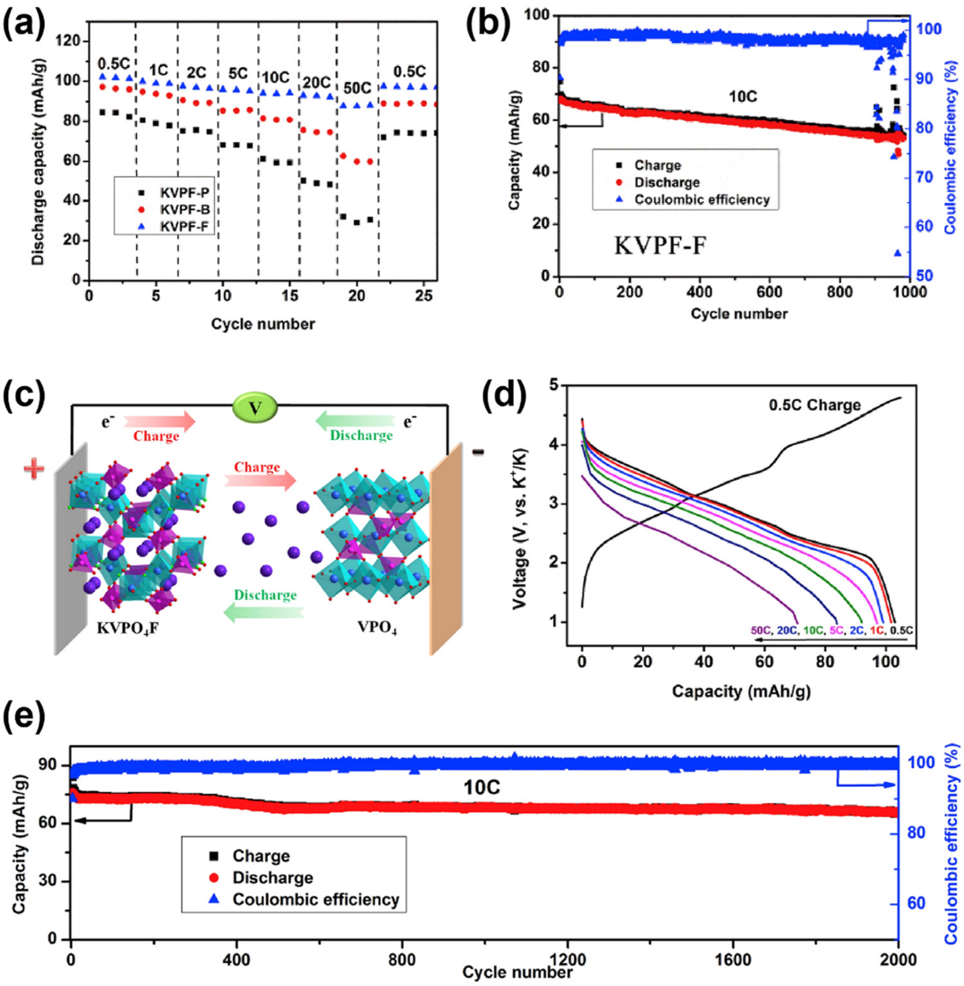

Fig. 14 (a) Rate performance of KVPF-based cathode. (b) Cycling performance of KVPF-F cathode. (c) Schematic representation, (d) rate performance, and (e) cycling performance of KVPF||VPO_4 full cell. Reproduced with permission.[156] Copyright 2020, Elsevier.

cyclability of 86% capacity retention over 200 cycles when assembled with hard carbon. Under the protection of the surface coating, the integrity of the $KVPO_4F$ could be well preserved without other side reactions.[157] Liu *et al.* designed and synthesized a KVPF@3DC cathode inspired by the special construction of a plum-pudding model *via* front-mounted ball-milling and subsequent calcination. In the so-called plum-pudding model structure, the $KVPO_4F$ particles referring to plums were uniformly wrapped by amorphous carbon and firmly bridged by a 3D conductive network formed by carbon sheets and overall surrounded by a flow of electrons. The carbon layer acted as a protector between the electrolyte/electrode interface, preventing the electrode from being eroded by the electrolyte and its decomposition at high voltage and elevated temperature, ensuring the high purity of the $KVPO_4F$ particles. The conductive network provided a fast charge transfer channel, significantly enhancing the electron/Na-ion migration kinetics. The as-prepared $KVPO_4F$@3DC cathode demonstrated excellent long-term cyclability with 85.4% capacity retention over cycles at 500 mA g^{-1}. Additionally, $KVPO_4F$@3DC showed excellent high temperature (55 °C) K^+-storage by maintaining 84% of its initial capacity at 50 mA g^{-1} after 100 cycles.[154]

In addition, heteroatomic doping is an effective modification approach for the $KVPO_4F$ material. Recently, Wernert *et al.* investigated the effect of the single partial replacement of fluorine with O^{2-} in the $KVPO_4F$ material. The simultaneous existence of ionic V^{3+}–F bonds and covalent $(V^{4+}{=}O)^{2+}$ vanadyl-type entities strongly affected the electrochemical properties and K^+ (de)insertion mechanisms upon cycling. Consequently, the optimized $KVPO_4F_{0.5}O_{0.5}$ cathode demonstrated significant application prospects in PIBs with a large initial capacity of 105 mA h g^{-1} and a high voltage plateau of 4.2 V.[64] Byeon *et al.* investigated the effect of Ti^{4+} and O^{2-} on $KVPO_4F$ materials, and the results showed that both Ti^{4+} and O^{2-} substitution led to smoothing of the associated voltage profile as well as reduced charging time at a high voltage (>4.8 V *vs.* K/K^+). These changes effectively suppressed the decomposition of the electrolyte, thereby enhancing the capacity retention of the $KV_{(1-x)}Ti_xPO_{4+y}F_{1-y}$ materials in the PIBs.[158]

3.2.2 $K_3V_2(PO_4)_2F_3$ and $K_3V_2O_2(PO_4)_2F$. In addition to the commonly reported $KVPO_4F$ material, the rare $K_3V_2(PO_4)_2F_3$

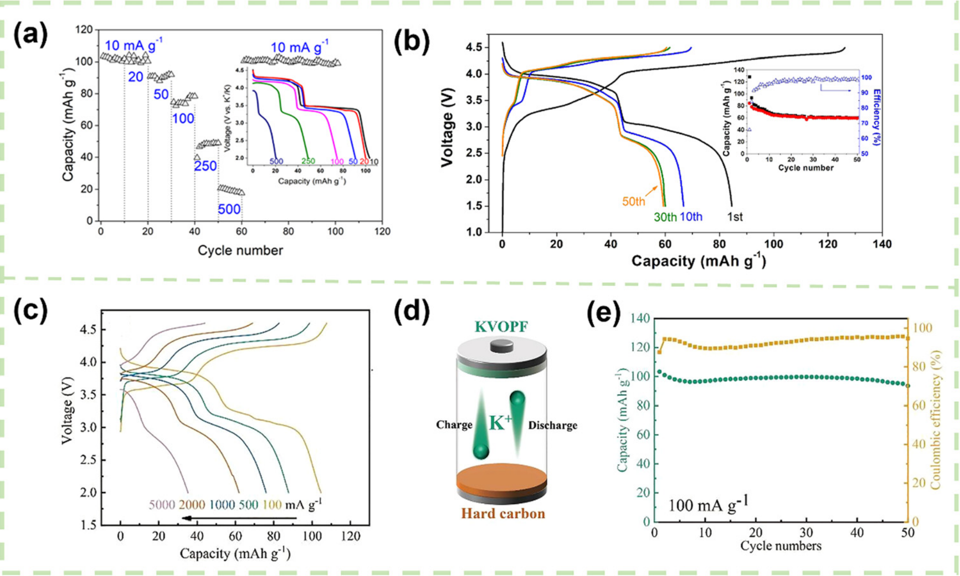

Fig. 15 (a) Rate capability of $K_3V_2(PO_4)_2F_3$ (inset: discharge curves at vary current density). (b) GCD curves of $K_3V_2(PO_4)_2F_3$ (inset: cycling performance). Reproduced with permission.[159] Copyright 2019, Elsevier. (c) GCD curves at different current densities and (d) schematic representation and (e) cyclability of KVPOF full batteries. Reproduced with permission.[160] Copyright 2022, Elsevier.

and $K_3V_2O_2(PO_4)_2F$ materials have also been studied. Lin *et al.* reported the preparation of a robust K-storage cathode material, *i.e.*, $K_3V_2(PO_4)_2F_3$, *via* a solid-state method. As shown in Fig. 15a, the novel KVPF cathode delivered 100 mA h g^{-1} at 10 mA g^{-1}, and maintained a distinct charge/discharge plateau (3.3–3.4 V). Moreover, the as-assembled $K_3V_2(PO_4)_2F_3$||graphite full cell could reach a high working plateau of 3.4 V, delivering an initial capacity of 84 mA h g^{-1} and maintaining 59 mA h g^{-1} after 50 cycles (Fig. 15b). The irreversible capacity was mainly caused by the formation of an SEI on the graphite anode. Subsequently, *in situ* XRD demonstrated the volume expansion of only 6.2% during cycling, which greatly explained the origin of its stability.[159] Zhang *et al.* first reported the preparation of a micron-sized $K_3V_2O_2(PO_4)_2F$ (KVOPF) cathode, which was synthesized *via* simple Na/K ion exchange using $Na_3V_2O_2(PO_4)_2F$, surprisingly realizing a great capacity and rate performance without extra carbon coating. This novel KVOPF cathode could deliver 105 mA h g^{-1} at 100 mA g^{-1} and 62 mA h g^{-1} at 2 A g^{-1} (Fig. 15c) and the lifespan of over 200 cycles. Finally, the KVPOF-HC full cell assembled using the KVPOF cathode and hard carbon anode (Fig. 15d) delivered 103.3 mA h g^{-1} and maintained a capacity retention of 90.5% for 50 cycles, which proved the potential of the KVOPF cathode (Fig. 15e). Moreover, the DFT calculations results revealed that the diffusion activation energy of K^+ transport in KVOPF was in the same order of magnitude as that for Na^+ transport in NVOPF, which is the reason for the high rate capacity.[160]

4. Electrochemical performance at low temperature

At present, there some regions such as areas near the Arctic Circle exhibit an extreme low temperature (LT) environment. Owing to the influence of LT, the properties of batteries have changed such as the efficiency and lifespan of batteries at LT, which are much lower than that in room temperature (RT). The normal use of electricity in these low-temperature environments has become a major problem, and thus low-temperature efficient working secondary batteries need to be developed. In this case, the most significant challenge to overcome is the diffusion of Na/K ions and the transmission of electrons at LT, which are much slower than that at RT condition; furthermore, the viscosity of the electrolyte in the battery increases and freezing may occur, which leads to the greater obstruction of ion transport at LT, resulting in a poor rate performance and unsatisfactory cyclability of the batteries.[161–167] Consequently, many efforts have been devoted to the fabrication of LT SIBs (PIBs) over the past few decades. Recently, with the deepening of research, more cathode and anode materials for LT SIBs have been reported. In the case of electrode materials with excellent properties at LT, the anode materials are mainly represented by transition metal sulfides ($CoGa_2S_4$,[168] FeS@g-C,[169] FeS_2@G@CNF[170] and ZnS-MWCNTs[171]), sodium titanium phosphate ($NaTi_2(PO_4)_3$@C,[172] NTP@C,[173] and NTP@C-CNTs[174]) and hard carbon (biomass-derived hard carbon[175] and hard carbon paper[176]), and the representatives of cathode materials mainly include sodium vanadium phosphate (laminated $Na_3V_2(PO_4)_3$,[177] $Na_3V_2(PO_4)_3$@C[178] and NVP/C-F[179]), Prussian blue and its analogues (PB/CNT[180] and $Na_2Ni[Fe(CN)_6]$[181]) and vanadium fluorophosphate materials. Among the vanadium fluorophosphate family members, stoichiometric $Na_3V_2(PO_4)_2F_3$ and $Na_3V_2O_2(PO_4)_2F$ are often used as research objects, while there are few reports on $NaVPO_4F$ and K-based vanadium fluorophosphate materials.[182,183] The progress on sodium vanadium fluorophosphates (*e.g.*, NVPF and NVPF) as cathode materials for half/full cells at LT is introduced here.

$Na_3V_2(PO_4)_2F_3$@rGO encapsulated in a 3D graphene network was successfully prepared *via* the hydrothermal strategy and calcination. Impressively, the $Na_3V_2(PO_4)_2F_3$@rGO cathode exhibited superior LT adaptability when tested at 0 °C, delivering 75 mA h g^{-1} after 180 cycles at 1C. The superior LT performance was attributed to its enhanced electron conductivity, fast Na^+ transport and structural stability.[184] Deng *et al.* proposed the strategy of controlling the pH value of the precursor solution to stabilize fluorine in the materials, thus eliminating the platforms presented at low voltages. The as-prepared $Na_3V_2(PO_4)_3F$ material displayed two clear plateaus at 3.6 V and 4.1 V without a low one at 3.3 V. After preventing the loss of fluorine and eliminating the influence of the low potential plateau, the structural stability and Na^+ migration kinetics of NVPF were enhanced, and its corresponding electrochemical properties were also improved. Particularly, the as-prepared $Na_3V_2(PO_4)_3F$ cathode showed great cycling stability at −25 °C, maintaining satisfactory capacity retention of 95.7% after 200 cycles at 44 mA g^{-1}.[185] Zhao *et al.* explored the temperature adaptability of the $Na_3V_2(PO_4)_3O_2F$ material, which showed a good performance in the wide temperature range of −25–55 °C. When cycled at 0.2C, the capacity retention of NVPOF at 0 °C and −25 °C was high as 99% and 86%, respectively, indicating that it is a good choice as a cathode for SIBs with excellent LT adaptability. The diffusion coefficients of Na^+ at 25 °C, 0 °C, and −25 °C calculated from the GITT curves were 10^{-13}–10^{-11}, 10^{-14}–10^{-11}, and 10^{-15}–10^{-12} cm^2 s^{-1}, respectively, proving that the diffusion coefficient tended to decrease with a decrease in temperature.[186] Guo *et al.* fabricated a tetra-prism-like nano-$Na_3V_2O_2(PO_4)_2F$ (Fig. 16a) with superior performance at room temperature, which significantly displayed outstanding LT adaptability. According to the GCD curves (Fig. 16b), the low-voltage platform was almost steeply sloped, while the high-voltage platform remained intact when tested at the LT of −15 °C. This phenomenon was related to the slower kinetics of Na^+ migration at the lower voltage platform.

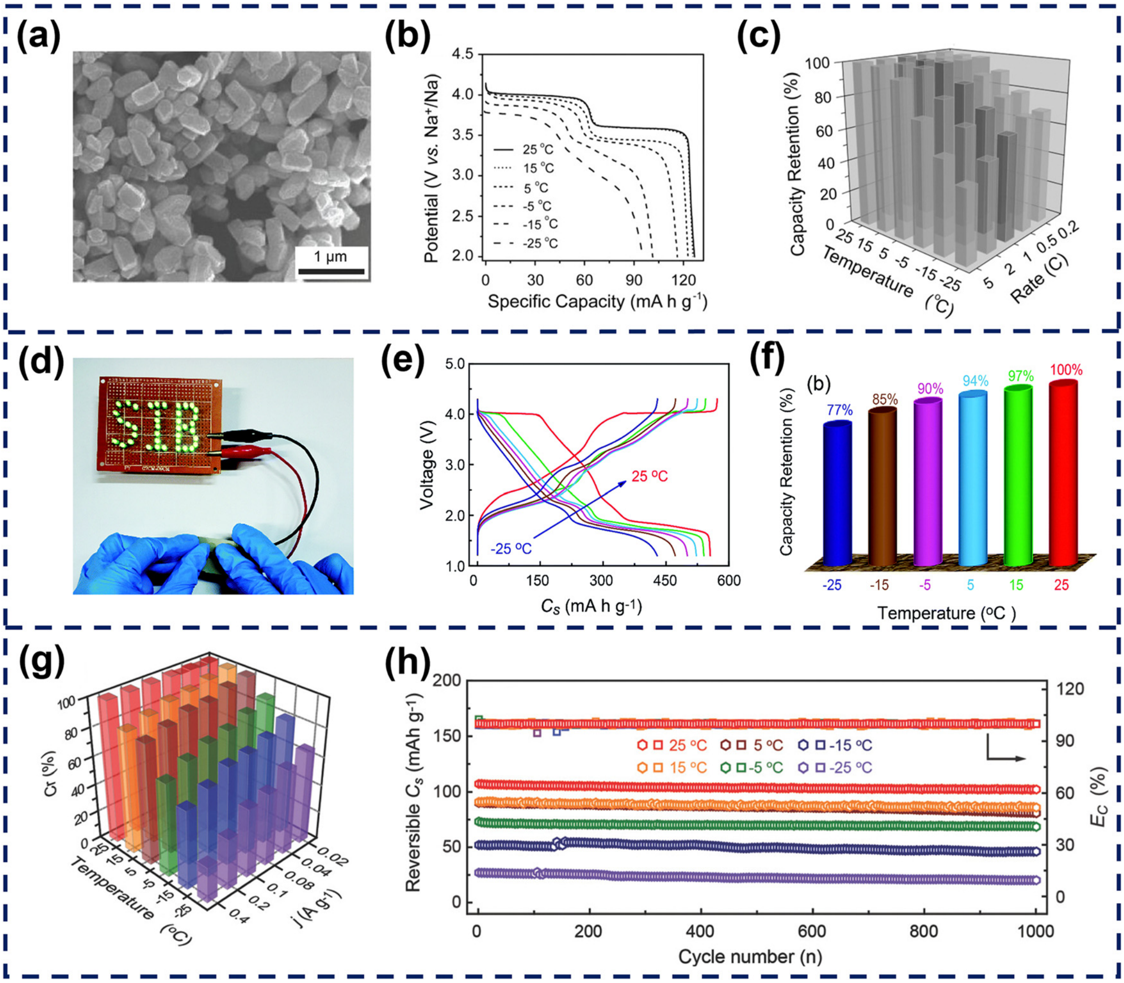

Fig. 16 (a) SEM of NVPOF-NTP. (b) Discharge curves of NVPOF-NTP cathode at different temperatures. (c) Capacity retention variation of NVPOF full cells as a function of rate and temperature. Reproduced with permission.[187] Copyright 2017, Wiley-VCH. (d) Digital photo of $Ni_{1.5}CoSe_5$@NC@rGO||NVPOF full cells. (e) GCD curves of $Ni_{1.5}CoSe_5$@NC@rGO||NVPOF full cells at different temperatures. (f) Capacity retention of $Ni_{1.5}CoSe_5$@NC@rGO||NVPOF full cells at different temperatures. Reproduced with permission.[188] Copyright 2018, The Royal Society of Chemistry. (g) Capacity retention variation as a function of *j* and temperature. (h) Cycling performance of 3DSG||NVPOF full batteries at different temperatures. Reproduced with permission.[189] Copyright 2018, Wiley-VCH.

Unexpectedly, all the curves presented two distinct plateaus even when tested at −25 °C and showed a discharge capacity of 96.1 mA h g^{-1}, which corresponded to a capacity retention of 76.4% compared to that at RT, and even when cycled at 5C, the capacity retention was still 44% of that tested at RT (Fig. 16c).[187] Moreover, $Na_3V_2O_2(PO_4)_2F$ is often regarded as an ideal cathode material for assembling full batteries. The assembled full batteries exhibited an extraordinary electrochemical performance even at sub-zero temperature. Wang *et al.* prepared an $Ni_{1.5}CoSe_5$@NC@rGO anode material and assembled a sodium ion full battery (SIFB) with $Na_3V_2O_2(PO_4)_2F$ as the cathode, which lit a series of LEDs (Fig. 16d) and was tested at different low temperatures (−5 °C, −15 °C and −25 °C). The electrochemical performance of SIFB showed 90%, 85% and 77% retention at −5 °C, −15 °C and −25 °C, respectively, when compared with the performance at 25 °C (Fig. 16e and f).[188] The same group also designed an SIFB with the as-prepared 3D Se/graphene anode and $Na_3V_2O_2(PO_4)_2F$ cathode. Consequently, a satisfactory LT electrochemical performance was achieved at −25 °C, especially long cycling stability with virtually no capacity degradation after hundreds of cycles at 100 mA g^{-1} and the capacity retention of 75% after ultra-long 1000 cycles at 400 mA g^{-1} (Fig. 16g and h).[189] Fan *et al.* reported the fabrication of an Fe_7Se_8@C||NVPOF full battery and tested it at −25 °C, which exhibited a high capacity of 165.6 mA h g^{-1} even after 440 cycles at 50 mA g^{-1} with a columbic efficiency of ∼99%. Surprisingly, the assembled full battery could light up 27 LEDs at −25 °C, strongly proving its practical value at LT.[190] This excellent LT capability mainly originated from the synergistic effect of the following aspects: sufficient reaction area with short diffusion channels in coral-like structure, fast electronic conduction in the carbon skeleton, and high working voltage and stabilization in the NVPOF positive side.

5. Conclusions

MVPF cathode materials are regarded as a prospective alternative for high-performance next-generation batteries due to their advantages of fast ion transportation and robust structure. However, their low intrinsic conductivity results in an unsatisfactory electrochemical performance including inferior rate capability and short working lifespan, severely limiting their further development in large-scale energy storage systems. Thus, to overcome these issues, various strategies such as conductive coating, morphological regulation and heteroatomic doping have been applied to enhance the properties of MVPF cathodes. In this review, the progress on the research related to the crystal structure and Na(K) storage mechanism of various MVPF materials, and the modification methods for developing high-performance MVPF cathodes were summarized. Moreover, the electrochemical performances of MVPF at subzero temperature were also discussed. Although significant progress has been made from the perspective of developing high-performance MVPF, multiple issues and challenges remain, which need to be addressed. The key prospects of vanadium fluorophosphate cathodes are suggested below.

(i) The practical applicability of MVPF still needs to be seriously improved. One is the large gap between its actual specific capacity and the theoretical capacity. Thus, the utilization of advanced characterization tools to reveal the underlying causes is critical, which can contribute to the further enhancement of its energy density, finally fulfilling the requirements of commercial applications. Additionally, the practical lifespan of vanadium fluorophosphate materials is much shorter than that of vanadium phosphate materials, with the realization of only a few thousand-long cycles, and thus there is still plenty of space for improvement in this regard.

(ii) Although the introduction of fluorine has a prominent contribution to its high working plateau with a consequent high energy density, the difficulties arising from it cannot be ignored. It is difficult to avoid the loss of fluorine in the synthesis of vanadium fluorophosphate materials obtained by high-temperature calcination, which may lead to high toxicity and cause the incorporation of additional oxygen, which can affect the purity, structure, and electrochemical properties of MVPF materials. It is necessary to effectively prevent the loss of fluorine in vanadium fluorophosphate compounds or introduce other elements to achieve the same effect without side reactions.

(iii) As a popular cathode material for SIBs/PIBs, there is still little research related to its performance at subzero temperature. Particularly, for K-based vanadium fluorophosphates, there are almost no relevant studies at low temperatures, and thus obvious shortcoming should not be underestimated. The intrinsic reasons for the difficulty in developing low-temperature PIBs must be uncovered.

It is believed that with the in-depth study of MVPF, high-performance vanadium fluorophosphate materials can be developed. We hope that progressive efforts will provide some effective inspiration, facilitating the development of vanadium-based polyanionic cathode materials and contributing to their movement towards practical applications.

Conflicts of interest

The authors declare no conflict of interest.

Acknowledgements

This work was supported by the National Natural Science Foundation of China (Grant No. 52222210, 51925207, U1910210, 52161145101, 51872277, 51972067, 51902062 and 52002083), the "Transformational Technologies for Clean Energy and Demonstration" Strategic Priority Research Program of Chinese Academy of Sciences (Grant No. XDA21000000), the National Synchrotron Radiation Laboratory (KY2060000173), the Joint Fund of the Yulin University and the Dalian National Laboratory for Clean Energy (Grant No. YLU-DNL Fund 2021002), the Fundamental Research Funds for the Central Universities (WK2060140026), Guangdong Natural Science Funds for Distinguished Young Scholar (Grant

No. 2019B151502039), and Fundamental Research Program of The Shenzhen Science and Technology Innovation Commission (Grant No. JCYJ20190809164209485).

References

1 X. B. Cheng, H. Liu, H. Yuan, H. J. Peng, C. Tang, J. Q. Huang and Q. Zhang, *SusMat*, 2021, **1**, 38–50.

2 M. Fan, X. Chang, Q. Meng, L. J. Wan and Y. G. Guo, *SusMat*, 2021, **1**, 241–254.

3 H. C. Jin, Y. S. Huang, C. N. Wang and H. X. Ji, *Small Sci.*, 2022, **2**, 2200015.

4 W. Xu, C. Tang, N. Huang, A. Du, M. Wu, J. Zhang and H. Zhang, *Small Sci.*, 2022, **2**, 2100105.

5 K. L. Guo, S. H. Qi, H. P. Wang, J. D. Huang, M. G. Wu, Y. L. Yang, X. Li, Y. R. Ren and J. M. Ma, *Small Sci.*, 2022, **2**, 2100107.

6 F. Zhao, S. Zhang, Y. Li and X. Sun, *Small Struct.*, 2021, **3**, 2100146.

7 Z. Shi, Z. Sun, X. Yang, C. Lu, S. Li, X. Yu, Y. Ding, T. Huang and J. Sun, *Small Sci.*, 2022, **2**, 2100110.

8 E. M. Hitz, H. Xie, Y. Lin, J. W. Connell, G. W. Rubloff, C.-F. Lin and L. Hu, *Small Struct.*, 2021, **2**, 2100014.

9 Q. Zhao, X. Chen, W. Hou, B. Ye, Y. Zhang, X. Xia and J. Wang, *SusMat*, 2022, **2**, 104–112.

10 L. Wu, Y. Wang, X. Guo, P. Ding, Z. Lin and H. Yu, *SusMat*, 2022, **2**, 264–292.

11 Q. Li, D. Yang, H. Chen, X. Lv, Y. Jiang, Y. Feng, X. Rui and Y. Yu, *SusMat*, 2021, **1**, 359–392.

12 D. Gong, C. Wei, Z. Liang and Y. Tang, *Small Sci.*, 2021, **1**, 2100014.

13 J. X. Ma, S. H. Zheng, P. Das, P. F. Lu, Y. Yu and Z. S. Wu, *Small Struct.*, 2020, **1**, 2000053.

14 S. Q. Chen, C. Wu, L. F. Shen, C. B. Zhu, Y. Y. Huang, K. Xi, J. Maier and Y. Yu, *Adv. Mater.*, 2017, **29**, 1700431.

15 L. N. Zhao and Z. H. Qu, *J. Energy Chem.*, 2022, **71**, 112–128.

16 J. Zhu, X. Chen, A. Q. Thang, F. L. Li, D. Chen, H. Geng, X. Rui and Q. Yan, *SmartMat*, 2022, **3**, 384–416.

17 F. Tang, R. Xia, D. Chen, Y. Yao, L. Liu, Y. Feng, X. Rui and Y. Yu, *J. Energy Chem.*, 2022, **74**, 1–7.

18 M. Huang, B. J. Xi, N. X. Shi, J. K. Feng, Y. T. Qian, D. F. Xue and S. L. Xiong, *Small Struct.*, 2021, **2**, 2000085.

19 C. Dong, F. Xu, L. Chen, Z. Chen and Y. Cao, *Small Struct.*, 2021, **2**, 2100001.

20 B. Tang, Y. Zhao, Z. Wang, S. Chen, Y. Wu, Y. Tseng, L. Li, Y. Guo, Z. Zhou and S.-H. Bo, *eScience*, 2021, **1**, 194–202.

21 D. Sun, S. Lin, D. Yu, Z. Wang, F. Deng, X. Zhou, G. Ma and Z. Lei, *Chin. Chem. Lett.*, 2022, **34**, 107339.

22 X. Xia, S. Xu, F. Tang, Y. Yao, L. Wang, L. Liu, S. He, Y. Yang, W. Sun, C. Xu, Y. Feng, H. Pan, X. Rui and Y. Yu, *Adv. Mater.*, 2022, e2209511, DOI: 10.1002/adma.202209511.

23 J. Tang, X. Peng, T. Lin, X. Huang, B. Luo and L. Wang, *eScience*, 2021, **1**, 203–211.

24 S. Ye, L. Wang, F. Liu, P. Shi and Y. Yu, *eScience*, 2021, **1**, 75–82.

25 X. Xia, C. F. Du, S. Zhong, Y. Jiang, H. Yu, W. Sun, H. Pan, X. Rui and Y. Yu, *Adv. Funct. Mater.*, 2021, **32**, 2110280.

26 Z. Hong, H. Maleki, T. Ludwig, Y. Zhen, M. Wilhelm, D. Lee, K.-H. Kim and S. Mathur, *J. Energy Chem.*, 2021, **62**, 660–691.

27 S. M. Ahmed, G. Suo, W. A. Wang, K. Xi and S. B. Iqbal, *J. Energy Chem.*, 2021, **62**, 307–337.

28 X. Lv, F. Tang, Y. Yao, C. Xu, D. Chen, L. Liu, Y. Feng, X. Rui and Y. Yu, *SusMat*, 2022, **2**, 699–707.

29 Z. Jinghan, L. Zeyu, J. Huaning, C. Qian, Y. Zhilin, G. Xiaokang, J. Yuying and G. Yongji, *SusMat*, 2022, **2**, 720–730.

30 Q. Deng, L. Wang, J. Li, Q. Cheng, X. Liu, C. Chen, Q. Zhang, W. Zhong, H. Wang, L. Wu and C. Yang, *Chin. Chem. Lett.*, 2022, **34**, 107372.

31 Z. Pan, X. Zhang, S. Xu, M. Gu, X. Rui and X. Zhang, *J. Mater. Chem. A*, 2023, **11**, 4102–4110.

32 W. Luo, F. Tang, Y. Jiang, L. Liu, W. Sun, Y. Feng, H. Pan, X. Rui and Y. Yu, *Adv. Funct. Mater.*, 2022, **32**, 2200178.

33 H. Kim, Y. Tian and G. Ceder, *J. Electrochem. Soc.*, 2020, **167**, 110555.

34 V. A. Nikitina, S. M. Kuzovchikov, S. S. Fedotov, N. R. Khasanova, A. M. Abakumov and E. V. Antipov, *Electrochim. Acta*, 2017, **258**, 814–824.

35 L. Ma, Y. Lv, J. Wu, C. Xia, Q. Kang, Y. Zhang, H. Liang and Z. Jin, *Nano Res.*, 2021, **14**, 4442–4470.

36 K. T. Yao, K. X. Zheng, L. Liu, H. Yu, S. L. Cheng and X. H. Rui, *ACS Appl. Mater. Interfaces*, 2022, **14**, 22389–22397.

37 Q. Chen, H. Li, H. Li, R. Wang, Q. Ma, L. Zhang and C. Zhang, *Chin. Chem. Lett.*, 2022, **34**, 107402.

38 Q. N. Liu, Z. Hu, W. J. Li, C. Zou, H. L. Jin, S. Wang, S. L. Chou and S. X. Dou, *Energy Environ. Sci.*, 2021, **14**, 158–179.

39 Q. N. Liu, Z. Hu, M. Z. Chen, C. Zou, H. L. Jin, S. Wang, S. L. Chou, Y. Liu and S. X. Dou, *Adv. Funct. Mater.*, 2020, **30**, 1909530.

40 J. Feng, S. Luo, K. Cai, S. Yan, Q. Wang, Y. Zhang and X. Liu, *Chin. Chem. Lett.*, 2022, **33**, 2316–2326.

41 Q. Wang, S. Chu and S. Guo, *Chin. Chem. Lett.*, 2020, **31**, 2167–2176.

42 R. Zhang, H. Chen and H. Yue, *Chin. Chem. Lett.*, 2022, **34**, 107580.

43 T. Jin, H. Li, K. Zhu, P. F. Wang, P. Liu and L. Jiao, *Chem. Soc. Rev.*, 2020, **49**, 2342–2377.

44 K. Liang, D. Wu, Y. Ren, X. Huang and J. Ma, *Chin. Chem. Lett.*, 2022, 107978, DOI: 10.1016/j.cclet.2022.107978.

45 Z. Lv, M. Ling, M. Yue, X. Li, M. Song, Q. Zheng and H. Zhang, *J. Energy Chem.*, 2021, **55**, 361–390.

46 J. F. Qian, C. Wu, Y. L. Cao, Z. F. Ma, Y. H. Huang, X. P. Ai and H. X. Yang, *Adv. Energy Mater.*, 2018, **8**, 1702619.

47 J. Peng, W. Zhang, Q. Liu, J. Wang, S. Chou, H. Liu and S. Dou, *Adv. Mater.*, 2022, **34**, e2108384.

48 X. Liu, Y. Cao and J. Sun, *Adv. Energy Mater.*, 2022, **12**, 2202532.

49 S. Zhao, Z. Guo, K. Yan, X. Guo, S. Wan, F. He, B. Sun and G. Wang, *Small Struct.*, 2020, **2**, 2000054.

50 S. Cao, H. Zhang, Y. Zhao and Y. Zhao, *eScience*, 2021, **1**, 28–43.

51 X. P. Yin, S. Sarkar, S. S. Shi, Q. A. Huang, H. B. Zhao, L. M. Yan, Y. F. Zhao and J. J. Zhang, *Adv. Funct. Mater.*, 2020, **30**, 1908445.

52 C. Zhang, C. B. Lu, F. Zhang, F. Qiu, X. D. Zhuang and X. L. Feng, *J. Energy Chem.*, 2018, **27**, 86–98.

53 Y.-F. Zhu, Y. Xiao, S.-X. Dou, Y.-M. Kang and S.-L. Chou, *eScience*, 2021, **1**, 13–27.

54 F. Wang, B. Peng, S. Zeng, L. Zhao, X. Zhang, G. Wan, H. Zhang and G. Zhang, *Adv. Funct. Mater.*, 2022, **32**, 2202665.

55 T. Liu, S. Hou, Y. Li, S. Xue, J. Hu, H. Fu, C. Yang and L. Zhao, *J. Energy Chem.*, 2022, **64**, 335–343.

56 W. Hua, X. Yang, N. P. M. Casati, L. Liu, S. Wang, V. Baran, M. Knapp, H. Ehrenberg and S. Indris, *eScience*, 2022, **2**, 183–191.

57 I. Sultana, M. M. Rahman, S. Mateti, N. Sharma, S. Huang and Y. Chen, *Batteries Supercaps*, 2020, **3**, 450–455.

58 X. Ma, J. Xia, X. Wu, Z. Pan and P. K. Shen, *Carbon*, 2019, **146**, 78–87.

59 J. Zhang, K. Jia, X. Li, X. Liu, L. Zhu and F. Wu, *J. Mater. Chem. A*, 2022, **10**, 10062–10068.

60 S. Chen, D. Zhao, L. Chen, G. Liu, Y. Ding, Y. Cao and Z. Chen, *Small Struct.*, 2021, **2**, 2100082.

61 Y. Liu, J. Li, Q. Shen, J. Zhang, P. He, X. Qu and Y. Liu, *eScience*, 2022, **2**, 10–31.

62 J. Liao, X. Zhang, Q. Zhang, Q. Hu, Y. Li, Y. Du, J. Xu, L. Gu and X. Zhou, *Nano Lett.*, 2022, **22**, 4933–4940.

63 Z.-Y. Gu, J.-Z. Guo, Z.-H. Sun, X.-X. Zhao, W.-H. Li, X. Yang, H.-J. Liang, C.-D. Zhao and X.-L. Wu, *Sci. Bull.*, 2020, **65**, 702–710.

64 R. Wernert, L. H. B. Nguyen, E. Petit, P. S. Camacho, A. Iadecola, A. Longo, F. Fauth, L. Stievano, L. Monconduit, D. Carlier and L. Croguennec, *Chem. Mater.*, 2022, **34**, 4523–4535.

65 Z. Jian, Y. S. Hu, X. Ji and W. Chen, *Adv. Mater.*, 2017, **29**, 1601925.

66 M. Mamoor, R. Lian, D. Wang, X. Meng, G. Chen and Y. Wei, *Phys. Chem. Chem. Phys.*, 2019, **21**, 14612–14619.

67 D. O. Semykina, I. V. Yakovlev, O. B. Lapina, A. A. Kabanov and N. V. Kosova, *Phys. Chem. Chem. Phys.*, 2020, **22**, 15876–15884.

68 S. D. Shraer, N. D. Luchinin, I. A. Trussov, D. A. Aksyonov, A. V. Morozov, S. V. Ryazantsev, A. R. Iarchuk, P. A. Morozova, V. A. Nikitina, K. J. Stevenson, E. V. Antipov, A. M. Abakumov and S. S. Fedotov, *Nat. Commun.*, 2022, **13**, 4097.

69 V. K. Kumar, S. Ghosh, V. Naresh, G. Ummethala, S. R. K. Malladi and S. K. Martha, *J. Electrochem. Soc.*, 2022, **169**, 010512.

70 M. Ling, Z. Lv, F. Li, J. Zhao, H. Zhang, G. Hou, Q. Zheng and X. Li, *ACS Appl. Mater. Interfaces*, 2020, **12**, 30510–30519.

71 M. Law and P. Balaya, *Energy Storage Mater.*, 2018, **10**, 102–113.

72 J. M. Le Meins, M. P. Crosnier-Lopez, A. Hemon-Ribaud and G. Courbion, *J. Solid State Chem.*, 1999, **148**, 260–277.

73 M. Bianchini, F. Lalère, H. B. L. Nguyen, F. Fauth, R. David, E. Suard, L. Croguennec and C. Masquelier, *J. Mater. Chem. A*, 2018, **6**, 10340–10347.

74 G. S. Mattei, J. M. Dagdelen, M. Bianchini, A. M. Ganose, A. Jain, E. Suard, F. Fauth, C. Masquelier, L. Croguennec, G. Ceder, K. A. Persson and P. G. Khalifah, *Chem. Mater.*, 2020, **32**, 8981–8992.

75 S. T. Dacek, W. D. Richards, D. A. Kitchaev and G. Ceder, *Chem. Mater.*, 2016, **28**, 5450–5460.

76 L. Zhu, H. Wang, D. Sun, Y. Tang and H. Wang, *J. Mater. Chem. A*, 2020, **8**, 21387–21407.

77 M. Bianchini, F. Fauth, N. Brisset, F. Weill, E. Suard, C. Masquelier and L. Croguennec, *Chem. Mater.*, 2015, **27**, 3009–3020.

78 G. Yan, S. Mariyappan, G. Rousse, Q. Jacquet, M. Deschamps, R. David, B. Mirvaux, J. W. Freeland and J. M. Tarascon, *Nat. Commun.*, 2019, **10**, 585.

79 A. Mukherjee, T. Sharabani, I. Perelshtein and M. Noked, *Batteries Supercaps*, 2019, **3**, 52–55.

80 M. Peng, X. Wang and G. Guo, *Appl. Mater. Today*, 2020, **19**, 100554.

81 A. A. Tsirlin, R. Nath, A. M. Abakumov, Y. Furukawa, D. C. Johnston, M. Hemmida, H. A. Krug von Nidda, A. Loidl, C. Geibel and H. Rosner, *Phys. Rev. B: Condens. Matter Mater. Phys.*, 2011, **84**, 014429.

82 N. Sharma, P. Serras, V. Palomares, H. E. A. Brand, J. Alonso, P. Kubiak, M. L. Fdez-Gubieda and T. Rojo, *Chem. Mater.*, 2014, **26**, 3391–3402.

83 C. Ma, T. Xu, C. Yan, J. Xu, D. Kong, Z. Zhang, W. Shen, Y. Shi, C. Ke, X. Li and Y. Wang, *J. Power Sources*, 2021, **482**, 228906.

84 M. Peng, D. Zhang, X. Wang, D. Xia, Y. Sun and G. Guo, *Chem. Commun.*, 2019, **55**, 3979–3982.

85 P. Serras, V. Palomares, T. Rojo, H. E. A. Brand and N. Sharma, *J. Mater. Chem. A*, 2014, **2**, 7766–7779.

86 K. Chihara, A. Katogi, K. Kubota and S. Komaba, *Chem. Commun.*, 2017, **53**, 5208–5211.

87 S. S. Fedotov, N. R. Khasanova, A. S. Samarin, O. A. Drozhzhin, D. Batuk, O. M. Karakulina, J. Hadermann, A. M. Abakumov and E. V. Antipov, *Chem. Mater.*, 2016, **28**, 411–415.

88 H. Tan, X. Du, J. Q. Huang and B. Zhang, *Chem. Commun.*, 2019, **55**, 11311–11314.

89 H. Kim, D. H. Seo, M. Bianchini, R. J. Clément, H. Kim, J. C. Kim, Y. Tian, T. Shi, W. S. Yoon and G. Ceder, *Adv. Energy Mater.*, 2018, **8**, 1801591.

90 H. Xu, Q. Yan, W. Yao, C.-S. Lee and Y. Tang, *Small Struct.*, 2022, **3**, 2100217.

91 D. Yang, S. Zhang, P. Yu, S. Cheng, Z. Yuan, Y. Jiang, W. Sun, H. Pan, Y. Feng, X. Rui and Y. Yu, *Small*, 2022, **18**, e2107058.

92 D. Chen, Y. Cheng, H. Pan, W. Sun, H. Geng and X. Rui, *Sci. China Mater.*, 2021, **65**, 646–652.

93 R. Zhao, N. Sun and B. Xu, *Small Struct.*, 2021, **2**, 2100132.

94 B. Wang, H. Cai, G. I. N. Waterhouse, X. Qu, B. Yang and S. Lu, *Small Sci.*, 2022, **2**, 2200012.

95 X. Zhang, D. Chen, Y. Zhou, D. Yang, W. Liu, Y. Feng, X. Rui and Y. Yu, *Chin. Chem. Lett.*, 2021, **32**, 1161–1164.

96 Y. Jiang, F. Guo, Y. Liu, Z. Xu and C. Gao, *SusMat*, 2021, **1**, 304–323.

97 C. Hakim, N. Sabi and I. Saadoune, *J. Energy Chem.*, 2021, **61**, 47–60.

98 Y. Li, M. Chen, B. Liu, Y. Zhang, X. Liang and X. Xia, *Adv. Energy Mater.*, 2020, **10**, 2000927.

99 C.-D. Zhao, J.-Z. Guo, Z.-Y. Gu, X.-X. Zhao, W.-H. Li, X. Yang, H.-J. Liang and X.-L. Wu, *J. Mater. Chem. A*, 2020, **8**, 17454–17462.

100 T. Jin, Y. Liu, Y. Li, K. Cao, X. Wang and L. Jiao, *Adv. Energy Mater.*, 2017, **7**, 1700087.

101 M. Ling, F. Li, H. Yi, X. Li, G. Hou, Q. Zheng and H. Zhang, *J. Mater. Chem. A*, 2018, **6**, 24201–24209.

102 X. Ge, X. Li, Z. Wang, H. Guo, G. Yan, X. Wu and J. Wang, *Chem. Eng. J.*, 2019, **357**, 458–462.

103 B. Cheng, S. Zhang, F. Zou, L. Luo, Y. Chen, S. Chen, H. Zhuo and X. Zeng, *J. Alloys Compd.*, 2019, **811**, 151828.

104 C. Chen, T. Li, H. Tian, Y. Zou and J. Sun, *J. Mater. Chem. A*, 2019, **7**, 18451–18457.

105 H. Zhuo, X. Wang, A. Tang, Z. Liu, S. Gamboa and P. J. Sebastian, *J. Power Sources*, 2006, **160**, 698–703.

106 P. Feng, W. Wang, J. Hou, K. Wang, S. Cheng and K. Jiang, *Chem. Eng. J.*, 2018, **353**, 25–33.

107 Y. U. Park, D. H. Seo, H. S. Kwon, B. Kim, J. Kim, H. Kim, I. Kim, H. I. Yoo and K. Kang, *J. Am. Chem. Soc.*, 2013, **135**, 13870–13878.

108 F. Li, Y. Zhao, L. Xia, Z. Yang, J. Wei and Z. Zhou, *J. Mater. Chem. A*, 2020, **8**, 12391–12397.

109 L. Deng, G. Sun, K. Goh, L.-L. Zheng, F.-D. Yu, X.-L. Sui, L. Zhao and Z.-B. Wang, *Electrochim. Acta*, 2019, **298**, 459–467.

110 T. Broux, F. Fauth, N. Hall, Y. Chatillon, M. Bianchini, T. Bamine, J. B. Leriche, E. Suard, D. Carlier, Y. Reynier, L. Simonin, C. Masquelier and L. Croguennec, *Small Methods*, 2018, **3**, 1800215.

111 H. Yi, L. Lin, M. Ling, Z. Lv, R. Li, Q. Fu, H. Zhang, Q. Zheng and X. Li, *ACS Energy Lett.*, 2019, **4**, 1565–1571.

112 L. L. Zhang, D. Ma, T. Li, J. Liu, X. K. Ding, Y. H. Huang and X. L. Yang, *ACS Appl. Mater. Interfaces*, 2018, **10**, 36851–36859.

113 W. X. Zhan, C. L. Fan, W. H. Zhang, G. D. Yi, H. Chen, S. C. Han and J. S. Liu, *Inter. J. Energy Res.*, 2020, **44**, 6608–6622.

114 A. Criado, P. Lavela, G. F. Ortiz, J. L. Tirado, S. Gzouli, Z. Edfouf and C. Pérez-Vicente, *Front. Phys.*, 2019, **7**, 207.

115 T. Wang, W. Zhang, H. Li, J. Hu, Y. Lai and Z. Zhang, *ACS Appl. Energy Mater.*, 2020, **3**, 3845–3853.

116 L. Zhu, Q. Zhang, D. Sun, Q. Wang, N. Weng, Y. Tang and H. Wang, *Mater. Chem. Front.*, 2020, **4**, 2932–2942.

117 Y. Li, X. Liang, G. Zhong, C. Wang, S. Wu, K. Xu and C. Yang, *ACS Appl. Mater. Interfaces*, 2020, **12**, 25920–25929.

118 Q. Liu, X. Meng, Z. Wei, D. Wang, Y. Gao, Y. Wei, F. Du and G. Chen, *ACS Appl. Mater. Interfaces*, 2016, **8**, 31709–31715.

119 S. Liu, X. Cao, Y. Zhang, K. Wang, Q. Su, J. Chen, Q. He, S. Liang, G. Cao and A. Pan, *J. Mater. Chem. A*, 2020, **8**, 18872–18879.

120 J. Olchowka, L. H. B. Nguyen, T. Broux, P. Sanz Camacho, E. Petit, F. Fauth, D. Carlier, C. Masquelier and L. Croguennec, *Chem. Commun.*, 2019, **55**, 11719–11722.

121 N. Pineda-Aguilar, V. J. Gallegos-Sánchez, E. M. Sánchez, L. C. Torres-González and L. L. Garza-Tovar, *J. Sol–Gel Sci. Technol.*, 2017, **83**, 405–412.

122 D. A. Puspitasari, J. Patra, I. M. Hung, D. Bresser, T.-C. Lee and J.-K. Chang, *ACS Sus. Chem. Eng.*, 2021, **9**, 6962–6971.

123 L. Li, Y. Xu, R. Chang, C. Wang, S. He and X. Ding, *Energy Storage Mater.*, 2021, **37**, 325–335.

124 J. Zhang, Y. Lai, P. Li, Y. Wang, F. Zhong, X. Feng, W. Chen, J. Liu, X. Ai, H. Yang and Y. Cao, *Green Energy Environ.*, 2021, **7**, 1253–1262.

125 L. Li, X. Liu, L. Tang, H. Liu and Y.-G. Wang, *J. Alloys Compd.*, 2019, **790**, 203–211.

126 A. Criado, P. Lavela, C. Pérez-Vicente, G. F. Ortiz and J. L. Tirado, *J. Electroanal. Chem.*, 2020, **856**, 113694.

127 C. Guo, J. Yang, Z. Cui, S. Qi, Q. Peng, W. Sun, L.-P. Lv, Y. Xu, Y. Wang and S. Chen, *J. Energy Chem.*, 2022, **65**, 514–523.

128 W. Liu, H. Yi, Q. Zheng, X. Li and H. Zhang, *J. Mater. Chem. A*, 2017, **5**, 10928–10935.

129 A. Mukherjee, Rosy, T. Sharabani, I. Perelshtein and M. Noked, *J. Mater. Chem. A*, 2020, **8**, 21289–21297.

130 J. Y. Park, Y. Shim, Y.-I. Kim, Y. Choi, H. J. Lee, J. Park, J. E. Wang, Y. Lee, J. H. Chang, K. Yim, C. W. Ahn, C.-W. Lee, D. K. Kim and J. M. Yuk, *J. Mater. Chem. A*, 2020, **8**, 20436–20445.

131 N. V. Kosova and D. O. Rezepova, *J. Power Sources*, 2018, **408**, 120–127.

132 H. Yi, M. Ling, W. Xu, X. Li, Q. Zheng and H. Zhang, *Nano Energy*, 2018, **47**, 340–352.

133 X. Shen, J. Zhao, Y. Li, X. Sun, C. Yang, H. Liu and Y.-S. Hu, *ACS Appl. Energy Mater.*, 2019, **2**, 7474–7482.

134 X. Shen, Q. Zhou, M. Han, X. Qi, B. Li, Q. Zhang, J. Zhao, C. Yang, H. Liu and Y. S. Hu, *Nat. Commun.*, 2021, **12**, 2848.

135 Z.-Y. Gu, J.-Z. Guo, Y. Yang, H.-Y. Yu, X.-T. Xi, X.-X. Zhao, H.-Y. Guan, X. He and X.-L. Wu, *Inorg. Chem. Front.*, 2019, **6**, 988–995.

136 W. Chang, X. Y. Zhang, J. Qu, Z. Chen, Y. J. Zhang, Y. Sui, X. F. Ma and Z. Z. Yu, *ACS Appl. Mater. Interfaces*, 2020, **12**, 41419–41428.

137 Y. Hou, K. Chang, Z. Wang, S. Gu, Q. Liu, J. Zhang, H. Cheng, S. Zhang, Z. Chang and Z. Lu, *Sci. China Mater.*, 2018, **62**, 474–486.

138 B. Deng, N. Yue, H. Dong, Q. Gui, L. Xiao and J. Liu, *Chin. Chem. Lett.*, 2021, **32**, 826–829.

139 L. L. Zhang, J. Liu, C. Wei, P. P. Sun, L. Gao, X. K. Ding, G. Liang, X. L. Yang and Y. H. Huang, *ACS Appl. Mater. Interfaces*, 2020, **12**, 3670–3680.

140 X. Li, S. Jiang, S. Li, J. Yao, Y. Zhao, T. Bashir, S. Zhou, S. Yang, W. Li, W. Zhu, T. Liu, J. Zhao and L. Gao, *J. Mater. Chem. A*, 2021, **9**, 11827–11838.

141 M. Peng, D. Zhang, L. Zheng, X. Wang, Y. Lin, D. Xia, Y. Sun and G. Guo, *Nano Energy*, 2017, **31**, 64–73.

142 M. Peng, B. Li, H. Yan, D. Zhang, X. Wang, D. Xia and G. Guo, *Angew. Chem., Int. Ed.*, 2015, **54**, 6452–6456.

143 P. Du, T. Li, X. Jiang, D. Wang and X. Zheng, *J. Alloys Compd.*, 2020, **814**, 152270.

144 L. Zheng, D. Zhang, X. Wang and G. Guo, *Appl. Mater. Today*, 2021, **23**, 101032.

145 Y. Qi, Z. Tong, J. Zhao, L. Ma, T. Wu, H. Liu, C. Yang, J. Lu and Y.-S. Hu, *Joule*, 2018, **2**, 2348–2363.

146 L. Zhao, X. Rong, Y. Niu, R. Xu, T. Zhang, T. Li, Y. Yu and Y. Hou, *Small*, 2020, **16**, e2004925.

147 L. Yue, C. Peng, C. Guoa, X. Zhou, G. Li, N. Wang, J. Zhang, J. Liu, Z. Bai and X. S. Zhao, *Chem. Eng. J.*, 2022, **441**, 136132.

148 J. Wang, J. Kang, Z. Y. Gu, Q. Liang, X. Zhao, X. Wang, R. Guo, H. Yu, C. F. Du and X. L. Wu, *Adv. Funct. Mater.*, 2021, **32**, 2109694.

149 P. R. Kumar, Y. H. Jung and D. K. Kim, *J. Solid State Chem.*, 2016, **21**, 223–232.

150 P. R. Kumar, Y. H. Jung, S. A. Ahad and D. K. Kim, *RSC Adv.*, 2017, **7**, 21820–21826.

151 T. Partheeban, B. Senthilkumar, V. Aravindan, S. Madhavi and M. Sasidharan, *ACS Appl. Energy Mater.*, 2021, **4**, 1387–1397.

152 X. Xiang, Q. Lu, M. Han and J. Chen, *Chem. Commun.*, 2016, **52**, 3653–3656.

153 V. Palomares, P. Serras, H. E. A. Brand, T. Rojo and N. Sharma, *J. Mater. Chem. A*, 2015, **3**, 23017–23027.

154 Z. Liu, J. Wang and B. Lu, *Sci. Bull.*, 2020, **65**, 1242–1251.

155 J. Xu, J. Liao, Y. Xu, J. Li, C. Zhu, J. Lin and X. Zhou, *J. Energy Chem.*, 2022, **68**, 284–292.

156 J. Liao, Q. Hu, X. He, J. Mu, J. Wang and C. Chen, *J. Power Sources*, 2020, **451**, 227739.

157 X.-D. He, L.-M. Zhang, C.-H. Jiang and C.-H. Chen, *Chem. Eng. J.*, 2022, **433**, 134634.

158 Y.-W. Byeon, M.-J. Gong, Z. Cai, Y. Sun, N. J. Szymanski, J. Bai, D.-H. Seo and H. Kim, *Energy Storage Mater.*, 2023, **57**, 81–91.

159 X. Lin, J. Huang, H. Tan, J. Huang and B. Zhang, *Energy Storage Mater.*, 2019, **16**, 97–101.

160 Z. Zhang, R. Wang, Z. Chen, X. Liu, Z. Liu, J. Zeng, X. Zhao, K. Peng, Q. Yao, X. Zhang, K. Shi, C. Zhu and X. Yan, *Chem. Eng. J.*, 2022, **436**, 135235.

161 L. Yan, Y.-E. Qi, X. Dong, Y. Wang and Y. Xia, *eScience*, 2021, **1**, 212–218.

162 X. Pang, B. An, S. Zheng and B. Wang, *J. Alloys Compd.*, 2022, **912**, 165142.

163 X. Wang, X. Yin, X. Feng, Y. Li, X. Dong, Q. Shi, Y. Zhao and J. Zhang, *Chem. Eng. J.*, 2022, **428**, 130990.

164 Q.-C. Wang, Q.-Q. Qiu, N. Xiao, Z.-W. Fu, X.-J. Wu, X.-Q. Yang and Y.-N. Zhou, *Energy Storage Mater.*, 2018, **15**, 1–7.

165 A. C. Thenuwara, P. P. Shetty, N. Kondekar, C. Wang, W. Li and M. T. McDowell, *J. Mater. Chem. A*, 2021, **9**, 10992–11000.

166 L.-F. Zhou, X.-W. Gao, T. Du, H. Gong, L.-Y. Liu and W.-B. Luo, *Chem. Eng. J.*, 2022, **435**, 134838.

167 K. Zheng, S. Xu, Y. Yao, D. Chen, L. Liu, C. Xu, Y. Feng, X. Rui and Y. Yu, *Chem. Commun.*, 2022, **58**, 10349–10352.

168 F. Mo, Z. Lian, B. Fu, Y. Song, P. Wang, F. Fang, Y.-N. Zhou, S. Peng and D. Sun, *J. Mater. Chem. A*, 2019, **7**, 9051–9058.

169 H.-H. Fan, H.-H. Li, J.-Z. Guo, Y.-P. Zheng, K.-C. Huang, C.-Y. Fan, H.-Z. Sun, X.-F. Li, X.-L. Wu and J.-P. Zhang, *J. Mater. Chem. A*, 2018, **6**, 7997–8005.

170 C. Chen, Y. Yang, X. Tang, R. Qiu, S. Wang, G. Cao and M. Zhang, *Small*, 2019, **15**, 1804740.

171 A. Fan, T. Hou, X. Sun, D. Xie, X. Li, N. Zhang, J. Guo, S. Jin, Y. Zhou, S. Cai and C. Zheng, *ChemElectroChem*, 2020, **7**, 1904–1913.

172 X. Zhang, M. Zeng, Y. She, X. Lin, D. Yang, Y. Qin and X. Rui, *J. Power Sources*, 2020, **477**, 228735.

173 Q. Hu, M. Yu, J. Liao, Z. Wen and C. Chen, *J. Mater. Chem. A*, 2018, **6**, 2365–2370.

174 L. Wang, B. Wang, G. Liu, T. Liu, T. Gao and D. Wang, *RSC Adv.*, 2016, **6**, 70277–70283.

175 X. Lin, X. Du, P. S. Tsui, J.-Q. Huang, H. Tan and B. Zhang, *Electrochim. Acta*, 2019, **316**, 60–68.

176 B. H. Hou, Y. Y. Wang, Q. L. Ning, W. H. Li, X. T. Xi, X. Yang, H. J. Liang, X. Feng and X. L. Wu, *Adv. Mater.*, 2019, **31**, e1903125.

177 Q. Zheng, W. Liu, X. Li, H. Zhang, K. Feng and H. Zhang, *J. Mater. Chem. A*, 2016, **4**, 19170–19178.

178 T. Kulova, *Int. J. Electrochem. Sci.*, 2019, **14**, 1451–1460.

179 X. Rui, X. Zhang, S. Xu, H. Tan, Y. Jiang, L. Y. Gan, Y. Feng, C. C. Li and Y. Yu, *Adv. Funct. Mater.*, 2020, **31**, 2009458.

180 Y. You, H. R. Yao, S. Xin, Y. X. Yin, T. T. Zuo, C. P. Yang, Y. G. Guo, Y. Cui, L. J. Wan and J. B. Goodenough, *Adv. Mater.*, 2016, **28**, 7243–7248.

181 X.-H. Ma, Y.-Y. Wei, Y.-D. Wu, J. Wang, W. Jia, J.-H. Zhou, Z.-F. Zi and J.-M. Dai, *Electrochim. Acta*, 2019, **297**, 392–397.

182 Y. Wang, X. Gao, L. Li, M. Wang, J. Shui and M. Xu, *Nano Energy*, 2020, **67**, 104248.

183 L. Deng, K. Goh, F.-D. Yu, Y. Xia, Y.-S. Jiang, W. Ke, Y. Han, L.-F. Que, J. Zhou and Z.-B. Wang, *Energy Storage Mater.*, 2022, **44**, 82–92.

184 Y. Cai, X. Cao, Z. Luo, G. Fang, F. Liu, J. Zhou, A. Pan and S. Liang, *Adv. Sci.*, 2018, **5**, 1800680.

185 L. Deng, F.-D. Yu, Y. Xia, Y.-S. Jiang, X.-L. Sui, L. Zhao, X.-H. Meng, L.-F. Que and Z.-B. Wang, *Nano Energy*, 2021, **82**, 105659.

186 X. X. Zhao, Z. Y. Gu, W. H. Li, X. Yang, J. Z. Guo and X. L. Wu, *Chemistry*, 2020, **26**, 7823–7830.

187 J. Z. Guo, P. F. Wang, X. L. Wu, X. H. Zhang, Q. Yan, H. Chen, J. P. Zhang and Y. G. Guo, *Adv. Mater.*, 2017, **29**, 201701968.

188 Y.-Y. Wang, H. Fan, B.-H. Hou, X.-H. Rui, Q.-L. Ning, Z. Cui, J.-Z. Guo, Y. Yang and X.-L. Wu, *J. Mater. Chem. A*, 2018, **6**, 22966–22975.

189 Y.-Y. Wang, B.-H. Hou, J.-Z. Guo, Q.-L. Ning, W.-L. Pang, J. Wang, C.-L. Lü and X.-L. Wu, *Adv. Energy Mater.*, 2018, **8**, 1703252.

190 H. H. Fan, H. H. Li, Z. W. Wang, W. L. Li, J. Z. Guo, C. Y. Fan, H. Z. Sun, X. L. Wu and J. P. Zhang, *ACS Appl. Mater. Interfaces*, 2019, **11**, 47886–47893.